Cell

Short-distance vesicle transport via phase separation

Graphical abstract

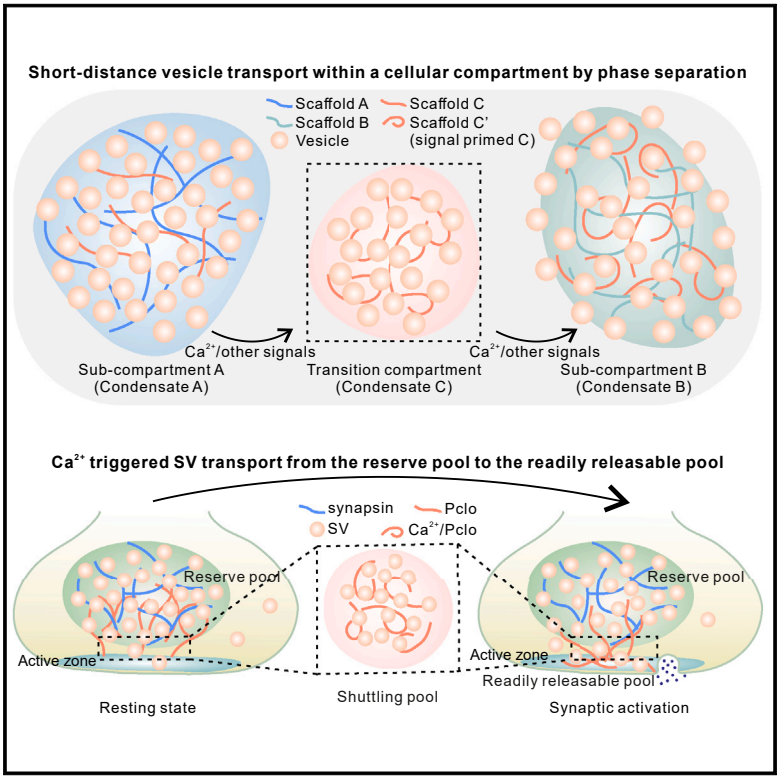

Highlights

- Scaffold protein Pclo extracts SVs from reserve pool condensate in response to Ca^{2+}
- Pclo enriches into the active zone condensate via binding to RIMBP and ELKS1
- Pclo promotes vesicle tethering on the surface of active zone condensate
- Ca^{2+} induces SV transport from reserve pool condensate to active zone condensate

Authors

Hua Qiu, Xiandeng Wu, Xiaoli Ma, ..., Liang Ge, Hong Zhang, Mingjie Zhang

Correspondence

zhangmj@sustech.edu.cn

In brief

Using the reconstituted presynaptic terminal local vesicle transport as a paradigm, Qiu and Wu et al. demonstrate that short-distance and directional vesicle transport can be achieved via regulated phase separation of vesicles with different protein condensates without involving molecular motors.

Qiu et al., 2024, Cell *187*, 1–19
April 25, 2024
https://doi.org/10.1016/j.cell.2024.03.003

CellPress

Please cite this article in press as: Qiu et al., Short-distance vesicle transport via phase separation, Cell (2024), https://doi.org/10.1016/j.cell.2024.03.003

Cell

CellPress

Article

Short-distance vesicle transport via phase separation

Hua Qiu,[1,11] Xiandeng Wu,[1,11] Xiaoli Ma,[2,8] Shulin Li,[3,9,10] Qixu Cai,[1,4] Marcelo Ganzella,[5] Liang Ge,[3,9,10] Hong Zhang,[2,8] and Mingjie Zhang[6,7,12,*]

[1]Division of Life Science, Hong Kong University of Science and Technology, Clear Water Bay, Kowloon, Hong Kong, China
[2]National Laboratory of Biomacromolecules, CAS Center for Excellence in Biomacromolecules, Institute of Biophysics, Chinese Academy of Sciences, Beijing 100101, China
[3]State Key Laboratory of Membrane Biology, Beijing, China
[4]State Key Laboratory of Molecular Vaccinology and Molecular Diagnostics, Department of Laboratory Medicine, School of Public Health, Xiamen University, Xiamen 361102, China
[5]Department of Neurobiology, Max Planck Institute for Biophysical Chemistry, Göttingen 37077, Germany
[6]Greater Bay Biomedical Innocenter, Shenzhen Bay Laboratory, Shenzhen 518036, China
[7]School of Life Sciences, Southern University of Science and Technology, Shenzhen 518055, China
[8]College of Life Sciences, University of Chinese Academy of Sciences, Beijing 100049, China
[9]Tsinghua-Peking Center for Life Sciences, Beijing 100084, China
[10]School of Life Sciences, Tsinghua University, Beijing 100084, China
[11]These authors contributed equally
[12]Lead contact
*Correspondence: zhangmj@sustech.edu.cn
https://doi.org/10.1016/j.cell.2024.03.003

SUMMARY

In addition to long-distance molecular motor-mediated transport, cellular vesicles also need to be moved at short distances with defined directions to meet functional needs in subcellular compartments but with unknown mechanisms. Such short-distance vesicle transport does not involve molecular motors. Here, we demonstrate, using synaptic vesicle (SV) transport as a paradigm, that phase separation of synaptic proteins with vesicles can facilitate regulated, directional vesicle transport between different presynaptic bouton subcompartments. Specifically, a large coiled-coil scaffold protein Piccolo, in response to Ca^{2+} and via its C2A domain-mediated Ca^{2+} sensing, can extract SVs from the synapsin-clustered reserve pool condensate and deposit the extracted SVs onto the surface of the active zone protein condensate. We further show that the Trk-fused gene, TFG, also participates in COPII vesicle trafficking from ER to the ER-Golgi intermediate compartment via phase separation. Thus, phase separation may play a general role in short-distance, directional vesicle transport in cells.

INTRODUCTION

Essentially, all vesicular trafficking processes involve directional movements of membranous vesicles with the required velocities to cope with different cellular needs.[1,2] Compared with biomolecules or their complexes, cellular vesicles are very large and heavy and thus diffuse extremely slowly in crowded cellular milieu.[3,4] Accordingly, directional, long-distance movements of vesicles between different cellular compartments always involve cytoskeletal-based molecular motors.[5–7]

Cellular vesicles also need to be transported locally with short distances. For example, distinct vesicles rapidly move both anterogradely and retrogradely along the flattened Golgi cisternae stacks with distances of a few hundred nanometers.[8,9] At the axon terminal boutons of nerve cells, synaptic vesicles (SVs) undergo rapid and repeated movements from vesicle reservoirs to the neurotransmitter release sites again with a distance of several hundred nanometers and in precisely timed intervals.[10–13] In contrast to the long-distance vesicle transport, very little is known regarding how local directional vesicle movements are achieved in cells. Such local, short-distance vesicle transports are not known to involve molecular motors. Random diffusion cannot account for such local but directional vesicle transports as random diffusion lacks directionality. Thus, certain process(es) must exist to actively facilitate the short-distance transportation of vesicles in local cellular compartments.

After long-distance, motor-mediated transport to each axonal terminal bouton,[14,15] mature SVs are organized into three subcompartments, corresponding to three distinct functional pools[16–19]: the reserve pool, which accounts for >80% of total SVs and is clustered at the presynaptic membrane-distal region; the readily releasable pool (RRP), which makes up <5% of total

Please cite this article in press as: Qiu et al., Short-distance vesicle transport via phase separation, Cell (2024), https://doi.org/10.1016/j.cell.2024.03.003

SVs and is attached to the active zone right beneath the presynaptic plasma membranes; and the recycling/shuttling pool, which is a rather imaginary population of SVs shuttling between the reserve pool and RRP. Upon synaptic activation, SVs from the reserve pool can be rapidly and repeatedly transported to the active zone to replenish released SVs. Such activity-induced SV transport does not involve molecular motors[20] as EM studies showed that the ~200–300 nm space between the active zone attached plasma membrane and the reserve pool SV is devoid of actin filaments or microtubules.[21,22]

Recent studies have shown that a set of presynaptic scaffold proteins or their complexes can form distinct condensed membraneless organelles via phase separation.[23–32] These presynaptic membraneless organelles interact with membranous SVs, each with a unique mode. For example, the synapsin and intersectin (ITSN) condensate can cluster SVs by coacervating with SVs.[25] SVs instead coat the surface of the active zone condensate formed by RIM, RIMBP, and ELKS.[26,29] Thus, these distinct presynaptic protein condensates could function to organize SVs into different pools and thereby define biochemically same SVs with distinct functions.[33,34] How SVs are transported from the reserve pool to RRP is currently unknown.

Piccolo (Pclo) and Bassoon are vertebrate-specific giant scaffold proteins (Pclo > 500 kDa; Bassoon > 400 kDa) capable of linking the active zone with the synapsin condensate (Figure S1A).[35–38] Ablations of Pclo and Bassoon lead to a significant reduction of total SVs, with both active-zone-docked and total recycling-pool SVs impaired.[39–43] By contrast, knockout of synapsin only impairs the reserve pool but not the docked SVs.[44,45] Knockout of RIM, RIMBP, and ELKS only affects RRP SVs without changing the reserve pool SVs.[46,47] The simultaneous impacts on multiple pools of SVs upon genetic manipulations of Pclo and/or Bassoon hint that these two scaffold proteins may coordinate the communications between different pools of SVs in presynaptic boutons.

Here, we discover that Pclo, in response to Ca^{2+} and via phase separation with SVs, can extract SVs from the synapsin-clustered condensate. Remarkably, Pclo can deliver the extracted SVs to the surface of the active zone condensate in a Ca^{2+}-dependent manner. Thus, Pclo can facilitate the transport of SVs from the reserve pool to the active zone via Ca^{2+}-regulated phase separation of presynaptic scaffold proteins. We also provide evidence that short-distance trafficking of secretory vesicles in cells is also regulated by protein phase separation.

RESULTS

PcloC extracts SVs from the reserve pool condensate in response to Ca^{2+}

We first validated that synapsin together with ITSN under a physiologically relevant condition underwent phase separation robustly (Figure S1B). Incubation of negatively charged small unilamellar vesicles (SUVs) composed of 77% POPC, 20% DOPS, 1% PI(4,5)P2, and 2% labeling dye (DiI here or DiD, DiO below) resulted in co-phase separation of synapsin/ITSN with SUVs, leading to clustering of SUVs in the synapsin condensate (Figure S1C). In synapses, SVs are mobilized from the reserve pool to RRP in response to Ca^{2+} to replenish the released ones.[48] However, in the absence of regulatory elements such as CaMKII,[25] the synapsin/SUV co-condensate by itself did not directly respond to Ca^{2+} (Figure S1D).

Since Pclo has been implied to contribute to SV mobilization, we asked whether Pclo might be involved in the SV organization in different compartments of synaptic boutons. Pclo is extremely large and modular. It contains two zinc-finger (ZF) domains at the N-terminal end, a PDZ domain and two C2 domains (C2A and C2B) at the C-terminal end, three predicted coiled-coil (CC) domains in the middle region, and a proline-rich motif (PRM) immediately preceding the third CC domain[49] (Figure S1E). All these domains are small (~100 aa) and separated by long, disordered linkers. A C-terminal segment starting from the PRM to the end of the protein is highly conserved among different species (Figure S1E). Additionally, this C-terminal segment of Pclo is suggested to point toward the presynaptic plasma membrane, interacting with the active zone proteins and playing a role in SV replenishment.[36,50–52] We were able to purify a Pclo fragment spanning PRM to the C-terminal end with the flexible linker between CC3 and PDZ removed to high purity and homogeneity (Figures S1E and S1F). We denote this fragment as PcloC hereafter (Figure S1E). Purified recombinant PcloC is a monomer in solution (Figure S1F).

We mixed PcloC with synapsin, ITSN, and SUV and found that PcloC was homogeneously partitioned into the synapsin/ITSN/SUV co-condensate (Figure 1A), likely due to SUV-mediated bindings to both PcloC and synapsin (Figure S1G). Remarkably, supplement of 1 mM Ca^{2+} in the assay buffer triggered dramatic redistributions of all components of the above mixture (Figure 1B). The distribution of PcloC became heterogeneous with only a small portion remaining colocalized with synapsin. The majority of PcloC coacervated with SUVs forming a distinct condensed phase surrounded by the synapsin phase (Figure 1B). Strikingly, almost all SUVs were extracted from the synapsin condensate and became co-clustered with the PcloC condensate (Figure 1B; quantified in Figure 1D). Upon stimulation, the intracellular Ca^{2+} concentration can reach dozens to 100 μM in presynaptic boutons.[53,54] We assayed Ca^{2+}-dependent vesicle extraction from the synapsin pool to the PcloC pool at Ca^{2+} concentrations ranging from 10 to 100 μM. Under all these Ca^{2+} concentrations, calcium triggered vesicle extraction from the synapsin condensate (Figures S1H–S1M), albeit that the level of vesicle extraction is lower than that with 1 mM Ca^{2+} used to saturate the C2A domain of PcloC (Figure S1N). The partial extraction of vesicles by PcloC at lower Ca^{2+} concentrations is aligned with the notion that only a few SVs need to be mobilized for exocytosis upon each synaptic stimulation.

SVs contain negatively charged lipids such as phosphatidylserine (PS) and phosphatidylinositol (PI), but the exact types and the concentrations of each lipids in SVs are not known.[55] Thus, we also tested Ca^{2+}-dependent vesicle extraction using two additional types of SUVs: one containing 20% DOPS (PS-SUV: 78% POPC + 20% DOPS + 2% DiI) and the other containing additional 1% PI3P (PI3P-SUV: 77% POPC + 20% DOPS + 1% PI3P + 2% DiI). Both types of SUVs behaved similarly to that of PI(4,5)P2-containing SUVs in our vesicle transport assays (Figures S2A–S2D).

Please cite this article in press as: Qiu et al., Short-distance vesicle transport via phase separation, Cell (2024), https://doi.org/10.1016/j.cell.2024.03.003

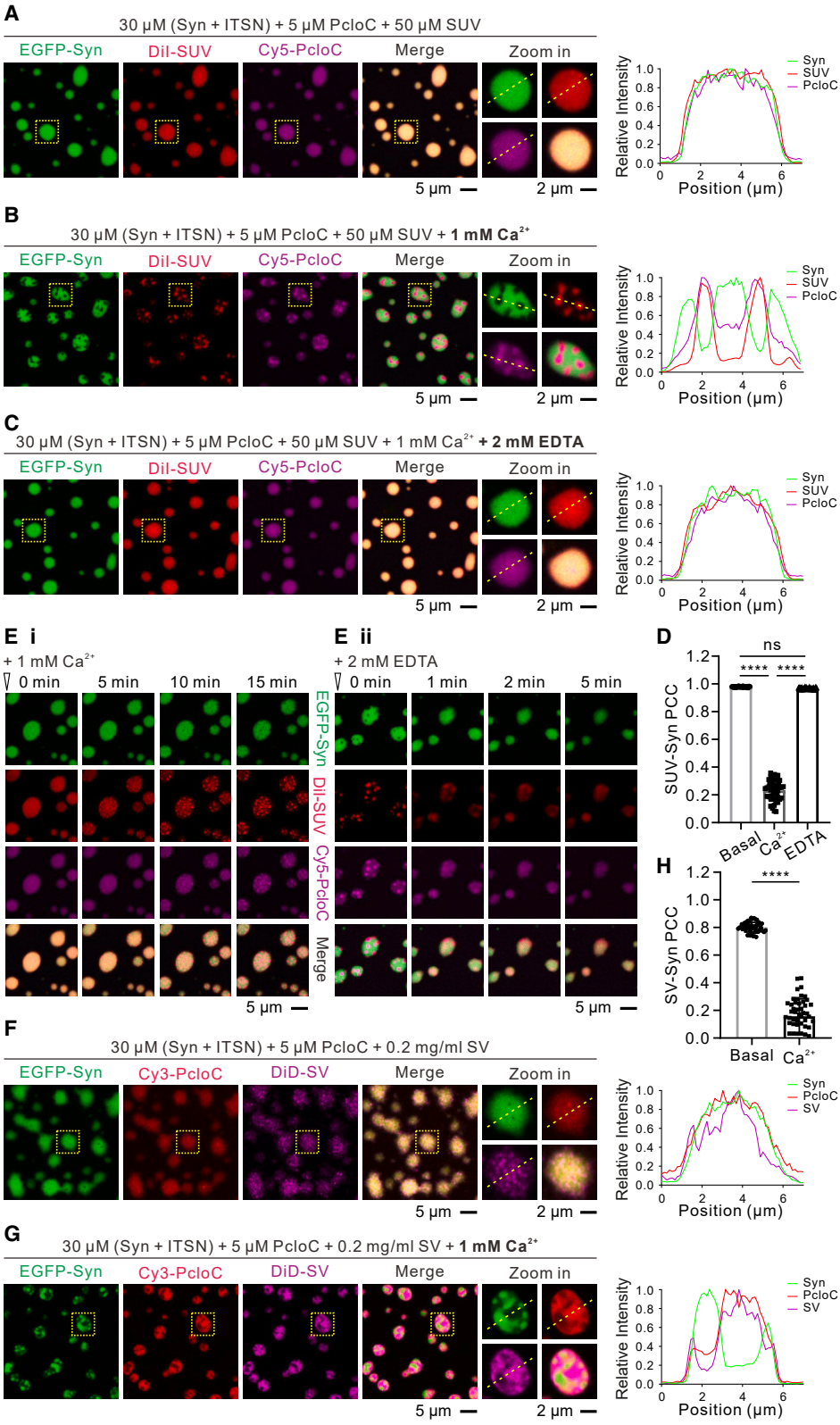

(legend on next page)

Please cite this article in press as: Qiu et al., Short-distance vesicle transport via phase separation, Cell (2024), https://doi.org/10.1016/j.cell.2024.03.003

This Ca^{2+}-induced redistribution of proteins and SUVs in different condensates is reversible, as chelation of Ca^{2+} by injecting 2 mM EDTA reversed the multiphase organization (Figure 1C; quantified in Figure 1D). Time-lapse imaging experiments captured the dynamic, Ca^{2+}-dependent, and reversible SUV extraction by PcloC from the synapsin/ITSN/SUV co-condensate (Figure 1E; Videos S1 and S2). Fluorescence recovery after photobleaching (FRAP) assay showed that PcloC in the newly formed condensate with SUVs after Ca^{2+} treatment remained highly mobile (Figure S2E). SUVs in different condensed phases are also mobile as illustrated by the observation that the SUV-containing PcloC droplets fused together upon contact with each other (Figure S2F). Additionally, treatments of SUV-containing condensates with Ca^{2+} or EDTA triggered redistributions of SUVs into different condensates (Figure 1E).

We then asked whether bona fide SVs might also undergo Ca^{2+}-dependent repartitioning from the synapsin condensate to the PcloC condensate. In the absence of Ca^{2+}, SVs purified from the rat brain were coacervated and clustered by the synapsin/ITSN/PcloC condensate. Slightly different from SUVs, SVs showed some micro-clustered pattern, but these micro-clusters were evenly distributed in the synapsin/ITSN/PcloC condensate (Figure 1F; quantified in Figure 1H). Injection of 1 mM Ca^{2+} dramatically changed the distribution pattern of SVs. Addition of Ca^{2+} caused SVs to be depleted in the synapsin condensate and with a concomitant formation of the PcloC/SV co-condensate segregated by the synapsin condensate (Figure 1G; quantified in Figure 1H). SVs are heavily decorated by proteins on their membrane surface.[55] We treated the purified SVs with trypsin to remove membrane surface proteins and then stopped the digestion reaction with aprotinin. Like the native SVs, the trypsin-digested SVs could also be extracted from the synapsin/ITSN condensate by PcloC to form a PcloC/SV co-condensate (Figures S2G–S2I), indicating that, in response to Ca^{2+} increase, PcloC mainly interacts with membrane lipids of SVs to induce SV moving from the synapsin condensate to the PcloC condensate.

PcloC undergoes phase separation with negatively charged vesicles in a Ca^{2+}-dependent manner

We next elucidated the molecular mechanism underlying Ca^{2+}-induced vesicle extraction from the synapsin condensate by PcloC. We found that mixing PcloC with negatively charged SUVs resulted in immediate formation of condensed droplets with PcloC and SUVs coacervated with each other (Figures 2Ai and 2Aiv for the quantification). By contrast, no condensate formation could be observed if PcloC was mixed with SUVs prepared with neutral lipids (Figures 2Aii and 2Aiv), indicating that negatively charged lipids on SUVs are essential for the phase separation of SUVs with PcloC. Addition of 1 mM of Ca^{2+} further promoted phase separation of PcloC with negatively charged SUVs (Figures 2Aiii and 2Aiv). Phase diagram analysis showed that phase separation between PcloC and SUVs could occur at the PcloC concentration as low as ~1 μM (Figure S3A). Increasing the concentration of either component promoted phase separation of the mixtures. Neither PcloC nor SUV alone was able to form any observable droplets (Figure S3A). The condensates formed by PcloC and SUVs are dynamic, as two droplets immediately coalesced and merged to a larger one upon contact (Figure 2B). FRAP assay showed that PcloC in the PcloC/SUV co-condensate is dynamic (Figure 2C).

We further dissected which elements in PcloC are responsible for Ca^{2+}-enhanced phase separation with SUVs. We found with surprise that the PRM and CC3 domains are required for PcloC to phase separate with SUVs, as the PDZ-C2A-C2B (PAB) tandem lacking PRM and CC3 could not form condensate with SUVs (Figure 2D; see also Figure 3). The fact that PcloC-PAB cannot phase separate with SUVs provided us with an opportunity to investigate the roles of the two Pclo-C2 domains in lipid binding and Ca^{2+} sensing using a high-speed sedimentation-based liposome binding assay (Figures S3B–S3D). Consistent with an earlier study,[56] the C2A domain underwent Ca^{2+}-dependent lipid binding (Figure S3D). Truncation of C2A or replacement of two Ca^{2+}-binding Asp residues in loop 1 (Figure S3B, termed as "$2DA_{C2A}$") barely affected basal lipid membrane binding of PAB (i.e., without Ca^{2+} in the assay buffer), and slightly but significantly weakened liposome binding ability in the presence of Ca^{2+} (Figure S3D). Though the structure of Pclo-C2B is not known, it is highly conserved and homologous to the C2B domain of RIM (Figure S3C), which does not bind to Ca^{2+}.[50,57,58] Like RIM-C2B, Pclo-C2B also binds to lipids (Figure S3D). Truncation of C2B or replacing two positively charged Lys in the β strand of Pclo-C2B with Glu (Figure S3C, termed as "$2KE_{C2B}$") eliminated the basal lipid binding capacity of PAB, but the PAB mutants could bind to liposomes in the presence of 1 mM Ca^{2+} due to Ca^{2+}-mediated lipid binding by C2A (Figure S3D). Thus, the C2B domain of Pclo can maintain lipid

Figure 1. PcloC extracts SVs from the reserve pool condensates in response to Ca^{2+}

(A) Confocal images showing the condensate formed by synapsin, ITSN, PcloC, and SUV at indicated concentrations. A dashed box is selected for zoom-in and by line-scanning analyses to show the distribution profiles of different components in the droplet. SUV composition: 77% POPC, 20% DOPS, 1% PI(4,5)P2, and 2% labeling dye. Protein labeling level: 5% for Pclo and 2% for the rest. Imaging buffer: 100 HEPES buffer saline containing 100 mM NaCl, 20 mM HEPES pH 7.5, and 1 mM TCEP (used throughout this study unless otherwise stated).

(B) Same protein and vesicle composition as in (A), but supplemented with 1 mM Ca^{2+} in the imaging buffer.

(C) Same composition as in (B), but with further addition of 2 mM EDTA.

(D) Quantification of Pearson's correlation coefficient (PCC) between SUV and synapsin for (A)–(C).

(E) Time-lapse images of Ca^{2+} (Ei) or EDTA (Eii) treatment of condensate formed by synapsin, ITSN, PcloC, and SUV. See also Videos S1 and S2.

(F and G) Representative images showing SVs distributions in the condensate formed by synapsin, ITSN, and PcloC, in the absence (F) or presence (G) of Ca^{2+}. Buffer condition: SV buffer contained 20 mM HEPES pH 7.5, 100 mM KCl, and 1 mM TCEP and was used in all experiments containing SVs. SVs were sparsely labeled by DiD.

(H) Quantification of PCC between SV and synapsin for (F) and (G).

All experiments presented here and below have been repeated at least three times using different batches of prepared proteins and vesicles. See also Figures S1 and S2.

Please cite this article in press as: Qiu et al., Short-distance vesicle transport via phase separation, Cell (2024), https://doi.org/10.1016/j.cell.2024.03.003

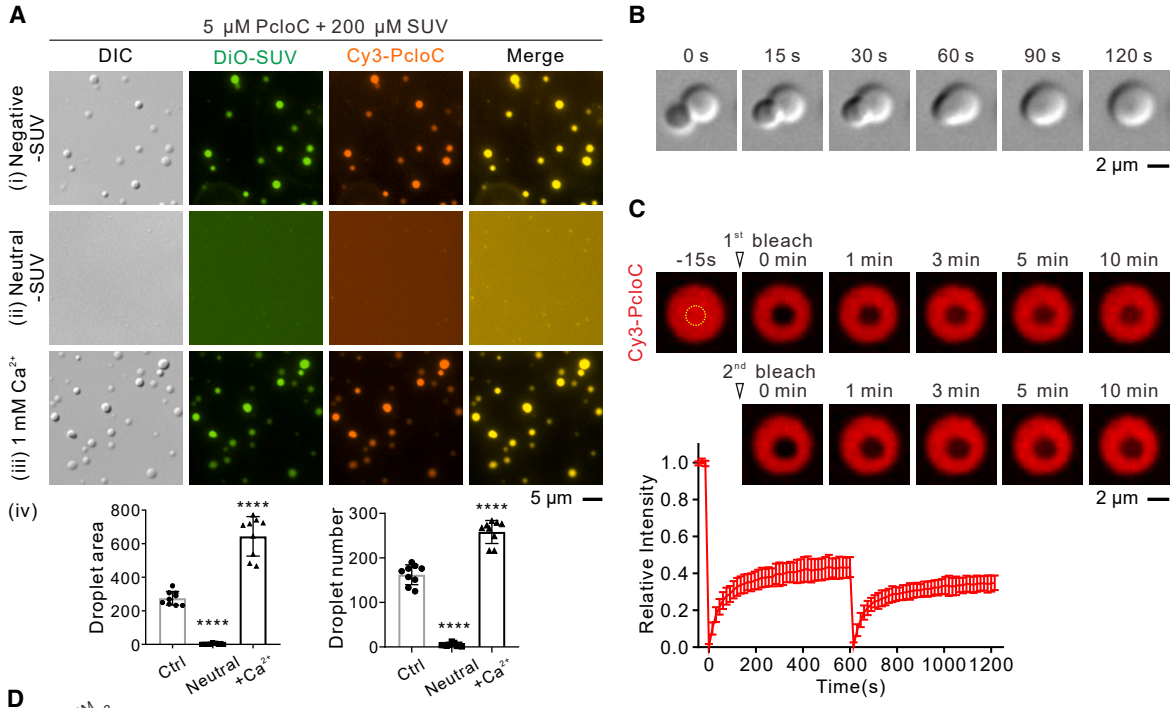

(legend on next page)

Please cite this article in press as: Qiu et al., Short-distance vesicle transport via phase separation, Cell (2024), https://doi.org/10.1016/j.cell.2024.03.003

membrane binding at the basal condition, and the C2A domain functions as a Ca^{2+} sensor to increase the interaction between Pclo and vesicles.

We then evaluated the roles of C2A and C2B domains in the phase separation of the PcloC/SUV mixtures. In the absence of Ca^{2+}, PcloC containing the $2KE_{C2B}$ mutation did not phase separate with SUVs, presumably due to the eliminated binding between the mutant PcloC and SUVs. Addition of Ca^{2+} promoted phase separation of PcloC-$2KE_{C2B}$ with SUVs, likely due to Ca^{2+}-mediated binding of C2A to SUVs. The $2DA_{C2A}$ mutation slightly increased PcloC/SUV phase separation under the basal condition (Figures 2D and S3E), presumably due to the removal of two negative charges in the mutant. Addition of Ca^{2+} did not promote but actually weakened phase separation of PcloC-$2DA_{C2A}$ with SUVs (Figures 2D and S3E), perhaps due to weakened interaction between the PcloC mutant and negatively charged lipid membranes caused by Ca^{2+}-mediated charge neutralization (Figure S3D). As expected, the quadruple mutant "$2DA_{C2A}$-$2KE_{C2B}$" was not able to phase separate with SUVs with or without Ca^{2+} (Figures 2D and S3E). Taking advantage of the above-identified mutations of PcloC, we were able to determine the elements of PcloC that are required to extract vesicles from the synapsin condensate. Under the basal condition, PcloC-$2KE_{C2B}$ can still partition into synapsin condensate (Figure 2E). Addition of Ca^{2+} only caused a very low-level co-enrichment of PcloC-$2KE_{C2B}$ with SUVs. The majority of SUVs and PcloC-$2KE_{C2B}$ were still formed co-condensates with synapsin and ITSN (Figure 2F; quantified in Figure 2I). In parallel, the PcloC-$2DA_{C2A}$ mutation did not affect its partition into synapsin condensate at the basal condition (Figure 2G). As expected, PlcoC-$2DA_{C2A}$ did not respond to Ca^{2+} in extracting SUVs from the synapsin condensate (Figure 2H; quantified in Figure 2I), as Ca^{2+} could not promote the binding of the PcloC mutant to lipid membranes (Figure S3D). Together, these findings revealed that both C2A and C2B of PcloC are required for PcloC to extract vesicles from the synapsin condensate.

PcloC enriches into the active zone condensate via direct binding to RIMBP and ELKS1

As an active zone component, Pclo is known to interact with multiple active zone proteins including RIM, RIMBP, ELKS1, Munc13, etc.[36,51] Consistently, we found that PcloC could be enriched into the active zone condensate formed by RIM, RIMBP, and ELKS1 (Figure 3A). However, once PRM and CC3 were removed, the remaining PAB tandem could no longer phase separate with the active zone condensate (Figure 3B), indicating that Pclo-PRM and CC3 are critical for its enrichment in the active zone condensate, likely via binding to active zone proteins.

RIMBP, via its SH3 domains, was reported to interact with the PRM of Bassoon.[59] We reasoned that RIMBP might also bind to Pclo-PRM, as PRMs of Bassoon and Pclo are highly similar. We purified Pclo-PRM and a RIMBP protein containing its three SH3 domains and measured their direct interaction using isothermal titration calorimetry (ITC). The apparent dissociation constant (K_D) of the interaction was ~4.0 μM and with a binding stoichiometry n of ~1.5 (Figure 3C), suggesting that more than one SH3 domains of RIMBP are involved in binding to Pclo. Further mapping showed that the first and third SH3 domains bind to Pclo, whereas the second SH3 did not bind to Pclo. The first SH3 has the strongest affinity for Pclo ($K_D \sim 0.74$ μM), and the third SH3 domain binds to Pclo with a weaker affinity ($K_D \sim 4.6$ μM) (Figure 3D). It is noted that the third SH3 domain of RIMBP binds to RIM-PRM with the strongest affinity, and the first SH3 domain binds to RIM with a weaker affinity.[26] Thus, the interactions of RIMBP to its PRM-containing partners are quite specific, and the three proteins can form a networked complex favorable for phase separation (Figure 3E).

Pclo has also been indicated to interact with ELKS,[60] though with an unclear molecular mechanism. The interaction between Pclo and ELKS was reported to be essential for their localizations in the active zone.[61,62] We mapped the Pclo/ELKS interaction (Figure S4A). Pclo-PRM-CC3 binds to ELKS1 with a strong affinity ($K_D \sim 0.31$ μM). Pclo-PRM-CC3 also binds to ELKS2, though with about a 10-fold lower affinity (Figure S4A). This indicates that Pclo and ELKS1 may function in SV shuttling, in line with a previous report showing that ELKS1 has a deeper localization in the presynaptic bouton overlapping with Pclo. By contrast, ELKS2 is more restricted at the near plasma membrane region.[63] We then focused on ELKS1 to investigate its interaction with Pclo. A predicted CC region (aa S469 to R610, termed as ELKS1-CC) of ELKS1 was mapped to be the minimal region for its binding to Pclo (Figure S4B). The two minimal fragments of Pclo (aa N3683 to S3769, termed as Pclo-CC3) and ELKS1-CC

Figure 2. PcloC undergoes phase separation with negatively charged vesicles in a Ca^{2+}-dependent manner

(A) Representative images showing that PcloC underwent phase separation with SUV. (Ai) PcloC phase separated with negatively charged SUV (77% POPC, 20% DOPS, 1% PI(4,5)P2, and 2% DiO). (Aii) PcloC could not form noticeable droplets with neutral SUV (98% POPC and 2% DiO). (Aiii) Additional 1 mM Ca^{2+} promoted phase separation of PcloC with negatively charged SUV. (Aiv) Quantification of droplet area and droplet number under conditions (Ai)–(Aiii). Data are presented as mean ± SD, ****$p < 0.0001$ using one-way ANOVA with Dunnett's multiple comparisons test.

(B) Time-lapse differential interference contrast (DIC) images showing the fusion process of two PcloC/SUV droplets.

(C) FRAP analysis of Cy3-labeled PcloC within a PcloC/SUV condensate. The dashed circle with a 10-pixel (pixel size = 0.13 μm) diameter inside a large droplet was selected for photobleaching. Droplets number n = 6 for the FRAP curve construction. Data are presented as mean ± SD.

(D) Summary of the phase separation level of PcloC with different boundaries or mutations with SUVs. Domain organizations and positions/schemes of the mutations are labeled in the corresponding schematic diagrams. Data are presented as mean ± SD. One-way ANOVA with Dunnett's multiple comparisons test was used. **$p < 0.01$; ***$p < 0.001$; ****$p < 0.0001$. See Figure S3 for the raw data.

(E and F) Representative images showing the condensates formed by synapsin, ITSN, PcloC-$2KE_{C2B}$, and SUV in the absence (E) or presence of 1 mM Ca^{2+} (F). A zoom-in image of a droplet is magnified at the lower left corner.

(G and H) Representative images showing the condensate formed by synapsin, ITSN, PcloC-$2DA_{C2A}$, and SUV in the absence (G) or presence of 1 mM Ca^{2+} (H).

(I) Quantification of PCC between SUV and synapsin for (E)–(H).

See also Figure S3.

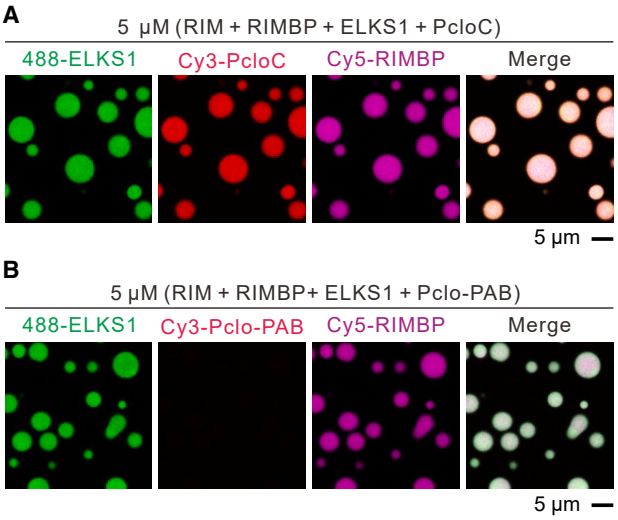

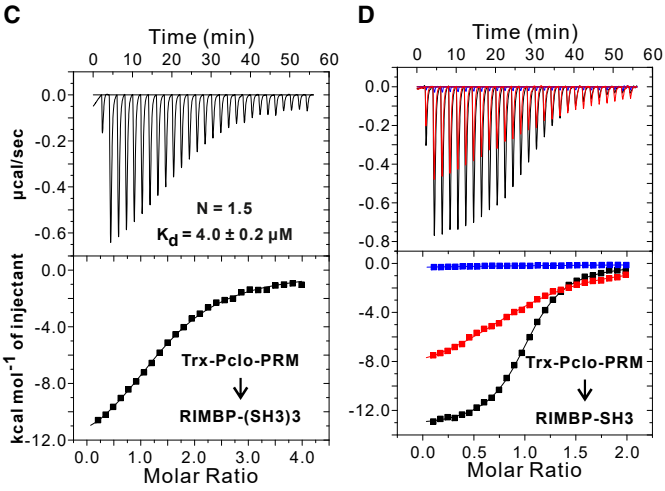

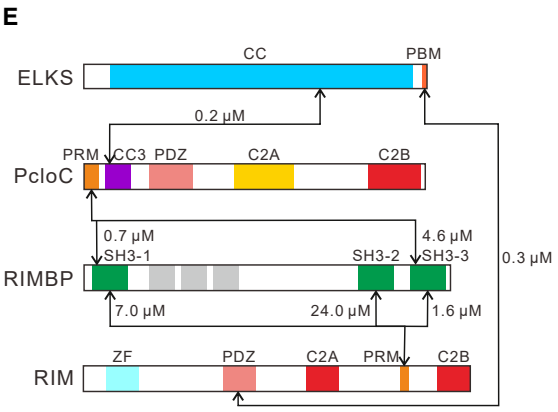

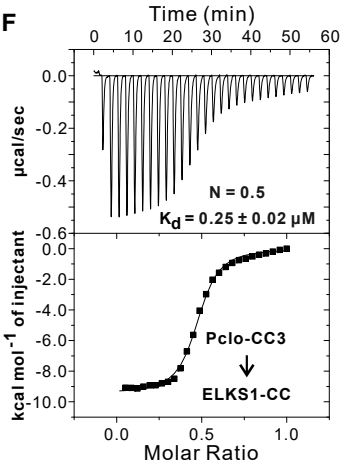

	k_d (μM)
RIMBP-1st SH3	0.74 ± 0.02
RIMBP-2nd SH3	N. D.
RIMBP-3rd SH3	4.63 ± 0.24

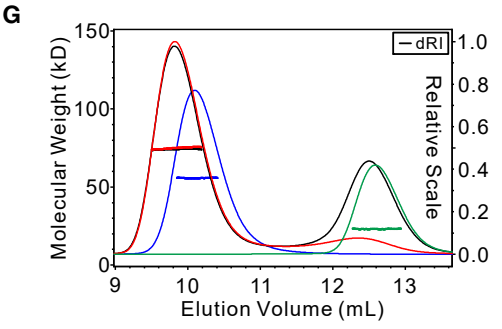

	Theoretical MW(kD)	Measured MW(kD)	Stoichiometry
Trx-ELKS1-CC (469-610)	31.0	55.7 ± 0.3	dimer
Trx-Pclo-CC3 (3683-3769)	24.8	23.1 ± 0.4	monomer
200 μM ELKS1-CC + 100 μM Pclo-CC3	-	75.1 ± 0.2	ELKS dimer+ Pclo monomer
200 μM ELKS1-CC + 200 μM Pclo-CC3	-	74.3 ± 0.2	ELKS dimer+ Pclo monomer

Figure 3. PcloC enriches into the active zone condensate via direct binding to RIMBP and ELKS1

(A and B) Confocal images showing that PcloC could be enriched into the RIM/RIMBP/ELKS1 condensate (A), whereas PcloC with PRM and CC3 removed ("PAB") could not (B).

(C and D) ITC experiments showing direct interaction between the Pclo-PRM and RIMBP-SH3 domain. (C) 200 μM Trx-tagged Pclo-PRM in the syringe was titrated into 10 μM RIMBP-(SH3)3 tandem in the cell. (D) 200 μM Trx-tagged Pclo-PRM in the syringe was titrated into 20 μM RIMBP-1st SH3 domain (black line), 20 μM RIMBP-2nd SH3 (blue line), or 20 μM RIMBP-3rd SH3 (red line) in the cell.

(E) A graphic scheme summarizing the interactions among active zone proteins RIM, RIMBP, ELKS1, and PcloC. Each two-way arrow line indicates one pair of interactions with the dissociation constant (K_D) derived from ITC marked.

(F) ITC assay showing the direct interaction between Pclo-CC3 and ELKS1-CC. 150 μM Pclo-CC3 (3,683–3,769) in the syringe was titrated into 30 μM ELKS1-CC (469–610) in the cell.

(G) SEC-MALS experiment showing a stable 2:1 complex formed by Pclo-CC3 and ELKS1-CC.

See also Figure S4.

Please cite this article in press as: Qiu et al., Short-distance vesicle transport via phase separation, Cell (2024), https://doi.org/10.1016/j.cell.2024.03.003

were found to interact with each other with an affinity comparable to that between two longest Pclo and ELKS1 fragments (Figures 3F vs. S4A). In ITC-based assays, we observed that ELKS1 binds to Pclo with a 2:1 stoichiometry (Figures 3F and S4). We showed that both PcloC (Figure S1F) and the CC3 domain of Pclo (Figure S4C) were stable monomers in solution, suggesting that Pclo-CC3 does not form a folded CC. Whereas ELKS1-CC is a stable dimer in solution (Figure 3G). The complex formed between ELKS1-CC and Pclo-CC3 has a molecular mass of ~75 kDa, corresponding to a dimer ELKS1-CC binding to a monomer Pclo-CC3 (Figure 3G).

Structural basis governing the specific interaction between ELKS1 and Pclo

To elucidate the molecular mechanism underlying the specific interaction between Pclo and ELKS1, we solved the structure of the Pclo-CC3/ELKS1-CC complex by X-ray crystallography (Table S1). The crystal structure confirmed that the Pclo-CC3/ELKS1-CC complex is composed of an ELKS1 dimer binding to a Pclo monomer (Figure 4A). In the complex, ELKS1-CC forms an elongated parallel CC (Figure 4A). The ELKS1-CC dimer is mainly stabilized by hydrophobic interactions between residues at the "c" and "g" positions of the heptad repeats (Figure 4B). Pclo-CC3 forms a single α helix and binds to the central part of the ELKS1 dimer in an anti-parallel manner, forming a three-helix bundle (Figure 4A). Pclo-CC3 only directly interacts with one chain (chain B in Figure 4) of the ELKS1-CC dimer, thus the complex is asymmetric. Both electrostatic and hydrophobic interactions govern the interaction between Pclo-CC3 and ELKS1-CC (Figures 4B–4D). Multiple salt bridges are critical for the strong and specific interaction between ELKS1-CC and Pclo-CC3 (dotted lines in Figure 4B; see also Figures 4C and 4D). Hydrophobic residues at the "c" and "f" positions of Pclo-CC3 also contribute to the complex formation (Figures 4B–4D). Point mutations disrupting these salt bridges or the hydrophobic interactions weakened or even abolished the interaction between ELKS1-CC and Pclo-CC3 (Figures 4E and 4F)

PcloC promotes vesicle tethering on the surface of active zone condensate

Since PcloC could cluster SUVs via phase separation by itself (Figure 2) and could also coacervate with the RIM/RIMBP/ELKS1 condensate (Figure 3), we asked whether PcloC might be able to promote vesicle tethering to the active zone condensate. We first verified that SUVs could coat the surface of the RIM/RIMBP/ELKS1 condensate (Figure 5A).[29] Then we examined the mixture of RIM, RIMBP, ELKS1, SUVs, and PcloC under the same imaging setting. All the proteins were homogeneously enriched in the condensate, whereas SUVs were retained on the surface of the protein condensate (Figure 5B). Strikingly, the density of SUVs coated on the condensate surface was dramatically increased upon addition of PcloC (Figure 5B; quantified in Figure 5D), suggesting that PcloC can facilitate vesicle tethering to the active zone surface. Next, we mixed the PcloC/SUV condensate with the RIM/RIMBP/ELKS1 condensate to probe what might occur when vesicles extracted by PcloC from the synapsin-clustered reserve pool meet the active zone condensate. The active zone condensate droplets composed of RIM, RIMBP, and ELKS1 were first formed in a glass chamber. PcloC/SUV condensate was then injected into the RIM/RIMBP/ELKS1 condensate. The subsequent reactions were monitored by time-lapse confocal imaging (Figure 5E; Video S3). When a PcloC/SUV droplet contacted with a RIM/RIMBP/ELKS1 droplet, PcloC immediately underwent time-dependent coacervation into the RIM/RIMBP/ELKS1 condensate, first with a ring-like structure at the outer region of and then fully mixed the RIM/RIMBP/ELKS1 droplets, accompanied with collapses of the PcloC/SUV droplets (Figure 5E). Remarkably, during the fusion of the PcloC/SUV droplets with the RIM/RIMBP/ELKS1 droplets, SUVs gradually spread on the surface of the RIM/RIMBP/ELKS1/PcloC condensate (Figure 5E). The above results indicate that vesicles originally clustered by PcloC are transferred to the surface of the active zone condensate due to preferred partitioning of PcloC into the active zone condensate.

We also found that Ca^{2+} could further enhance PcloC-mediated vesicle tethering on the surface of active zone condensate (Figures 5B vs. 5C; quantified in Figure 5D). The PcloC-$2DA_{C2A}$ Ca^{2+} sensing mutant could no longer respond to Ca^{2+} in promoting vesicle tethering onto the surface of active zone condensate (Figures S5A–S5C; quantified in Figure S5G); whereas the PcloC-$2KE_{C2B}$ mutant still showed Ca^{2+}-enhanced vesicle delivery to the active zone condensate surface (Figures S5D–S5F; quantified in Figure S5G).

We next investigated whether PcloC could enhance tethering of native SVs onto the active zone condensate surface. SVs purified from the rat brain could be tethered on the surface of the condensate formed by RIM, RIMBP, and ELKS1 (Figure 5F).[29] Addition of PcloC significantly increased the SV coating on the active zone condensate surface (Figure 5G; quantified in Figure 5I), and the tethering was further elevated by Ca^{2+} (Figures 5H and 5I). Again, this Ca^{2+}-induced SV tethering on active zone condensate surface was essentially eliminated by the PcloC-$2DA_{C2A}$ mutant, and the PcloC-$2KE_{C2B}$ mutant was still responsive to Ca^{2+} in promoting SV coating on the active zone condensate surface (Figures S5H–S5L).

Ca^{2+}-dependent, PcloC-mediated vesicle transport from the synapsin condensate to the active zone condensate

We next explored whether we might be able to reconstitute the Ca^{2+}-dependent vesicle transport process by mixing all above studied presynaptic proteins with vesicles. We first verified that the RIM/RIMBP/ELKS1 active zone condensate and the synapsin/ITSN condensate are immiscible with each other (Figure S6A). SUVs were homogeneously clustered in the synapsin condensate and coated on the surface of the active zone condensate (Figure 6A). Addition of PcloC led to its preferred partitioning into the active zone phase (Figure 6B) without altering the multiphase organization and vesicle distribution (Figure S6B). Strikingly, in response to Ca^{2+}, PcloC dramatically enhanced the coating of SUVs on the surface of the active zone condensate as illustrated by a bright ring-like SUV coating on the surface of each active zone droplet (Figure 6C). The fluorescence intensities of the SUV coat on the active zone droplets were much higher than the signals of vesicles within the synapsin condensate (Figure 6C; quantified in Figure 6D). The increase of

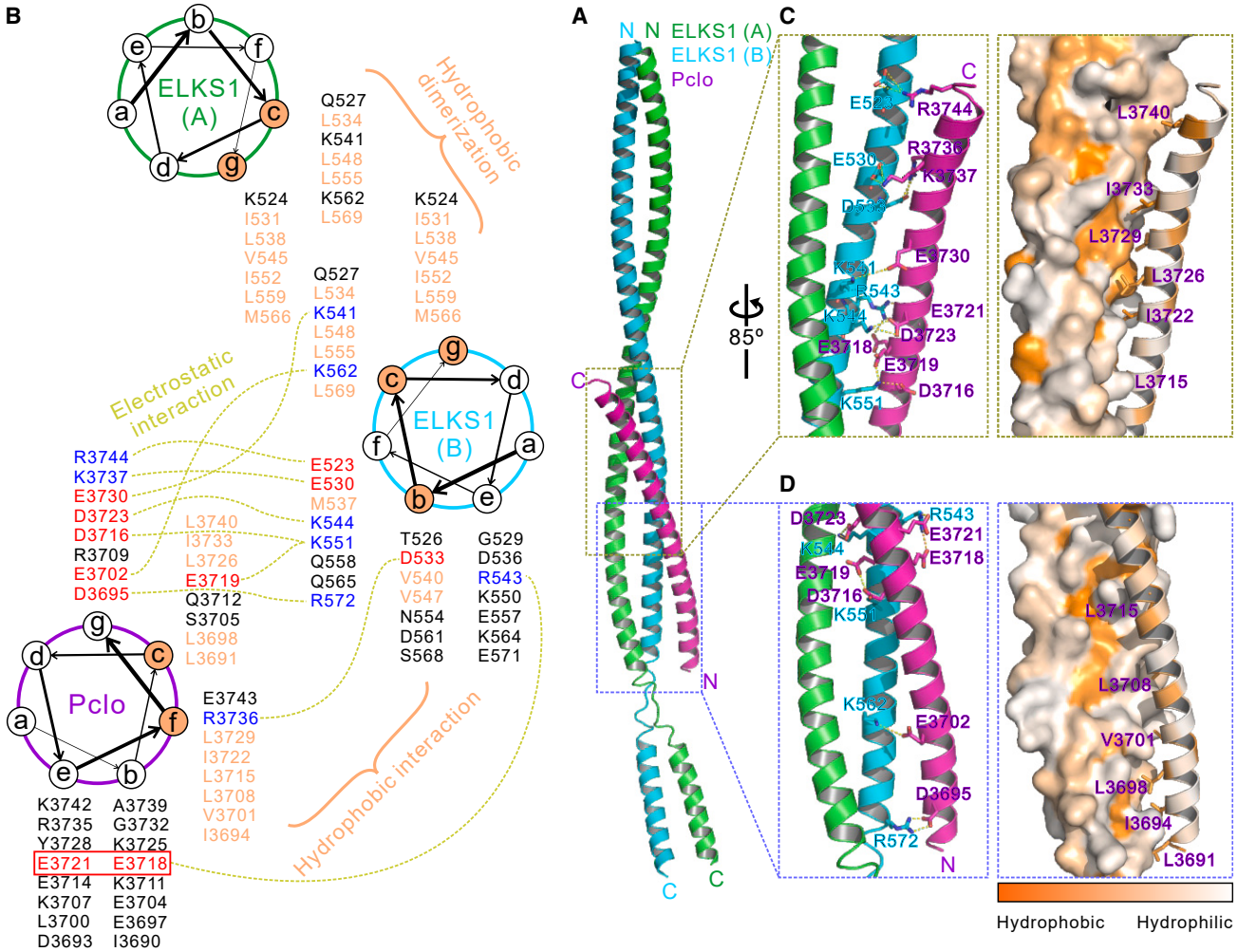

E

Pclo-CC3	ELKS1-CC	K_d(μM)
3683-3769		0.25 ± 0.02
D3695R (aggregation)		N.D.
E3719R (dimer)		8.55 ± 1.27
R3736D	469-610	2.26 ± 0.10
L3698R		0.71 ± 0.03
L3726R		3.94 ± 0.12
L3729E		N.D.

F

Pclo-CC3	ELKS1-CC	K_d(μM)
	D533R	1.70 ± 0.18
	R543D	0.40 ± 0.05
3683-3769	K544D	N.D.
	K551D	N.D.
	R572D	1.72 ± 0.07

Figure 4. Structural basis governing the interaction between ELKS1 and Pclo

(A) Cartoon representations of the overall structure of the ELKS1/Pclo complex.

(B) Helical wheel representation showing the interaction between ELKS1 and Pclo. The specific pairwise charge-charge interactions are indicated by dotted lines.

(C and D) The detailed electrostatic interactions (left panels shown with the ribbon model) and hydrophobic interactions (right panels drawn using the surface model) between ELKS1 and Pclo.

(E and F) Tables summarizing the ITC-based measurements of the binding affinities between variants of Pclo-CC3 and ELKS1-CC to validate the structure of the complex.

See also Table S1.

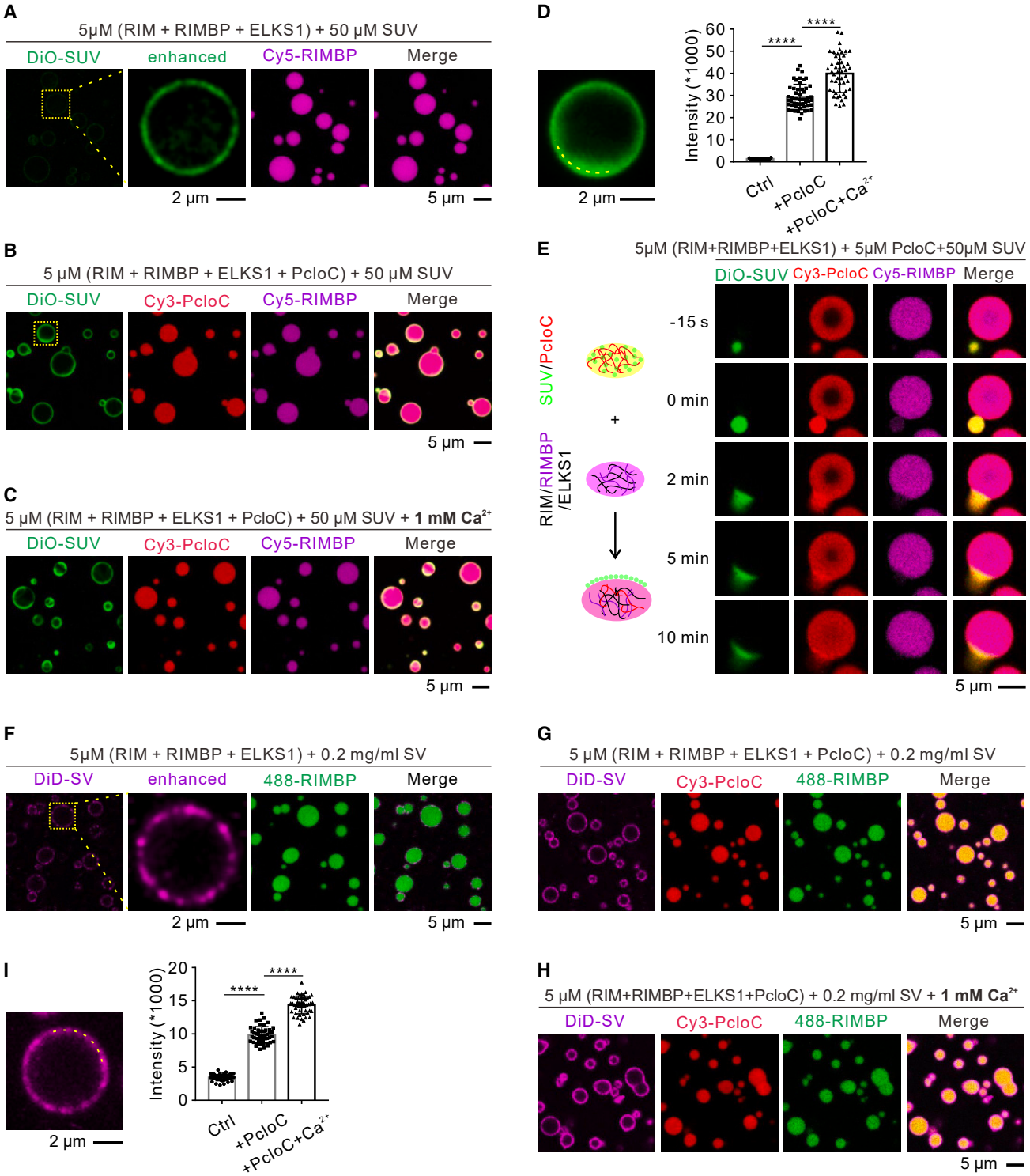

Figure 5. PcloC promotes vesicle tethering on the surface of the active zone condensate

(A) Representative images showing that SUVs coat on the surface of RIM/RIMBP/ELKS1 droplets. Imaging settings of (A)–(C) were exactly the same. All images used for comparison were taken within one imaging session. A zoom-in image with ~20-fold brightness enhancement to show that SUVs are coating on the surface of the RIM/RIMBP/ELKS1 droplets.

(B and C) Representative images showing that SUVs coat on the surface of RIM/RIMBP/ELKS1/PcloC droplets in the absence (B) or presence of 1 mM Ca^{2+} (C).

(legend continued on next page)

SUV intensity at the active zone droplet surface induced by Ca^{2+} is accompanied by decrease of vesicle signal in the synapsin phase (Figure S6C; Video S4), indicating that PcloC, in response to Ca^{2+} concentration rise, extracted vesicles from the synapsin-clustered pool and deposited these extracted vesicles to the surface of the active zone condensate. In the absence of PcloC, the reconstituted system shown in Figure 6A did not show any vesicle redistribution upon addition of Ca^{2+} (data not shown). Ca^{2+} elevation at the synapses is transient. To ask how fast Ca^{2+} can mobilize vesicles between different condensates, we preincubated all components except Ca^{2+} in the test tube for 15 min to ensure the system had reached an equilibrium. We added Ca^{2+} to the equilibrated sample mixture in the test tube and then immediately loaded the sample for imaging. In this case, SUVs were observed to be rapidly transported from synapsin condensate to the active zone condensate surface at the timescale of seconds (Figure S6D).

Fluorescence signals of PcloC and synapsin were rapidly recovered after photobleaching (Figure S6E), suggesting the overall mobility of entire system. Fluorescence signal of SUV was barely recovered (Figure S6E) due to the extremely large sizes of the SUVs. Vesicles in the synapsin condensate must be mobile, as otherwise there should be no vesicle redistribution to the surface of the active zone in response to Ca^{2+}.

Finally, we checked the role of the PcloC-$2DA_{C2A}$ and PcloC-$2KE_{C2B}$ mutants on vesicle transport between the synapsin condensate and the active zone condensate. Neither of the mutations influenced the multiphase organization of proteins and vesicles of the reconstituted presynaptic bouton (Figures S6F and S6G). In sharp contrast to wild-type (WT) PcloC, the PcloC-$2DA_{C2A}$ mutant could not extract SUVs from the synapsin condensate for depositing on the active zone condensate surface, presumably due to the loss of the Ca^{2+} sensing ability of the mutant (Figures 6E and 6F). As expected, the PcloC-$2KE_{C2B}$ mutant could still extract vesicles from the synapsin condensate and promote coating of vesicles on the surface of the active zone condensate in response to Ca^{2+} (Figures 6G and 6H).

TFG condensate in COPII vesicle trafficking

Sorting of COPII-coated vesicle from the ER to the ER-Golgi intermediate compartment (ERGIC) is another form of directed short-distance vesicle transport. Electron microscopic studies have revealed that COPII vesicles are confined and concentrated at the ER exit site,[64,65] though with an unknown molecular mechanism. Trk-fused gene (TFG) has been shown to facilitate COPII vesicle transport from the ER to the ERGIC,[65–68] which is also a form of directed short-distance vesicle transport. We hypothesized that protein phase separation may also participate in COPII vesicle trafficking, and TFG is such a candidate protein.

We first used grazing incidence structured illumination microscopy (GI-SIM) to image EGFP-tagged TFG stably expressed in COS7 cells (Figure S7A). As reported in an earlier study,[65] TFG appeared as numerous droplet-like puncta in the cytoplasm. These TFG droplets underwent continuous movements (Figure S7Bi) and could undergo fusion upon contact with each other (Figure S7Bii). Occasionally, large droplets could split into smaller ones (Figure S7Biii). These phenomena indicated that TFG droplets are mobile and with condensate-like properties. Transient expression of SEC23A, a marker of COPII vesicles, in the COS7 cell line stably expressing mCherry-TFG showed perfect colocalization of the TFG droplets with COPII vesicles (Figure 7A), suggesting that the TFG droplets can cluster COPII vesicles. Live cell GI-SIM imaging studies showed that SEC23A (and hence COPII vesicles) were always tightly associated with TFG droplets along the processes of TFG droplets movements, fusion, and fission (Figures 7Bi–7Biii).

We next characterized biochemical properties of purified TFG protein with or without EGFP or mCherry fusion tag. TFG appeared as a stable oligomer in solution by size exclusion chromatography coupled with multiangle light scattering (SEC-MALS) (Figures S6C and S6D), which is in line with an earlier report.[66] TFG alone rapidly formed spheric droplets at the protein concentration as low as 1 μM in the presence of 3% PEG8,000 to mimic molecular crowding of cytoplasmic milieu (Figure 7C). Similar to what was observed in COS7 cells, the TFG droplets readily fused into larger ones upon contact (Figure 7D). Thus, TFG can form condensed droplets via phase separation.

TFG contains an N-terminal PB1-like domain and a CC domain, followed by a long intrinsic disordered region (IDR). The N-terminal PB1-CC domain is responsible for its oligomerization.[65,66] We hypothesized that the specific multimerization of PB1-CC drives the phase separation of TFG, and the C-terminal IDR of the protein may further promote the phase separation property of the full-length protein.[69,70] Purified TFG-IDR was a stable monomer (Figure S7E). No obvious phase separation occurred for TFG-IDR in the presence of 3% PEG8,000 (Figure S7Fi). Nevertheless, when we increased the protein concentration to 100 μM in a buffer containing 10% PEG20,000, we did observe phase separation of TFG-IDR (Figure S7Fii), suggesting that the IDR may weakly promote phase separation of TFG.

We discovered that the TFG condensate perfectly coacervated with the negatively charged synthetic SUVs (Figures 7E

(D) Quantification and comparison of SUV coating efficiency among (A)–(C). The dashed box in (B) was selected as an example for fluorescence intensity analysis. 50 droplets from each group were analyzed for statistics. Unpaired t test was used. ****$p < 0.0001$.
(E) Time-lapse confocal images showing that the PcloC/SUV condensate can deposit vesicles to the surface of the active zone condensate. RIM/RIMBP/ELKS1 condensate was first settled down in a chamber. Preformed PcloC/SUV condensate was then injected into the chamber. The time point when two condensate droplets came into contact was set as 0 min. A schematic diagram showing the dynamic process is shown at the left. See also Video S3.
(F) Representative images showing that SVs coat on the surface of RIM/RIMBP/ELKS1 droplets. A dashed box was enlarged and with a ~3-fold brightness enhancement to show that SVs coat on the surface of the RIM/RIMBP/ELKS1 droplet.
(G and H) Representative images showing that SVs coat on the surface of RIM/RIMBP/ELKS1/PcloC droplets in the absence (G) or presence of 1 mM Ca^{2+} (H).
(I) Quantification and comparison of SV coating efficiency among (F)–(H) with the same method as in (D).
See also Figure S5.

Please cite this article in press as: Qiu et al., Short-distance vesicle transport via phase separation, Cell (2024), https://doi.org/10.1016/j.cell.2024.03.003

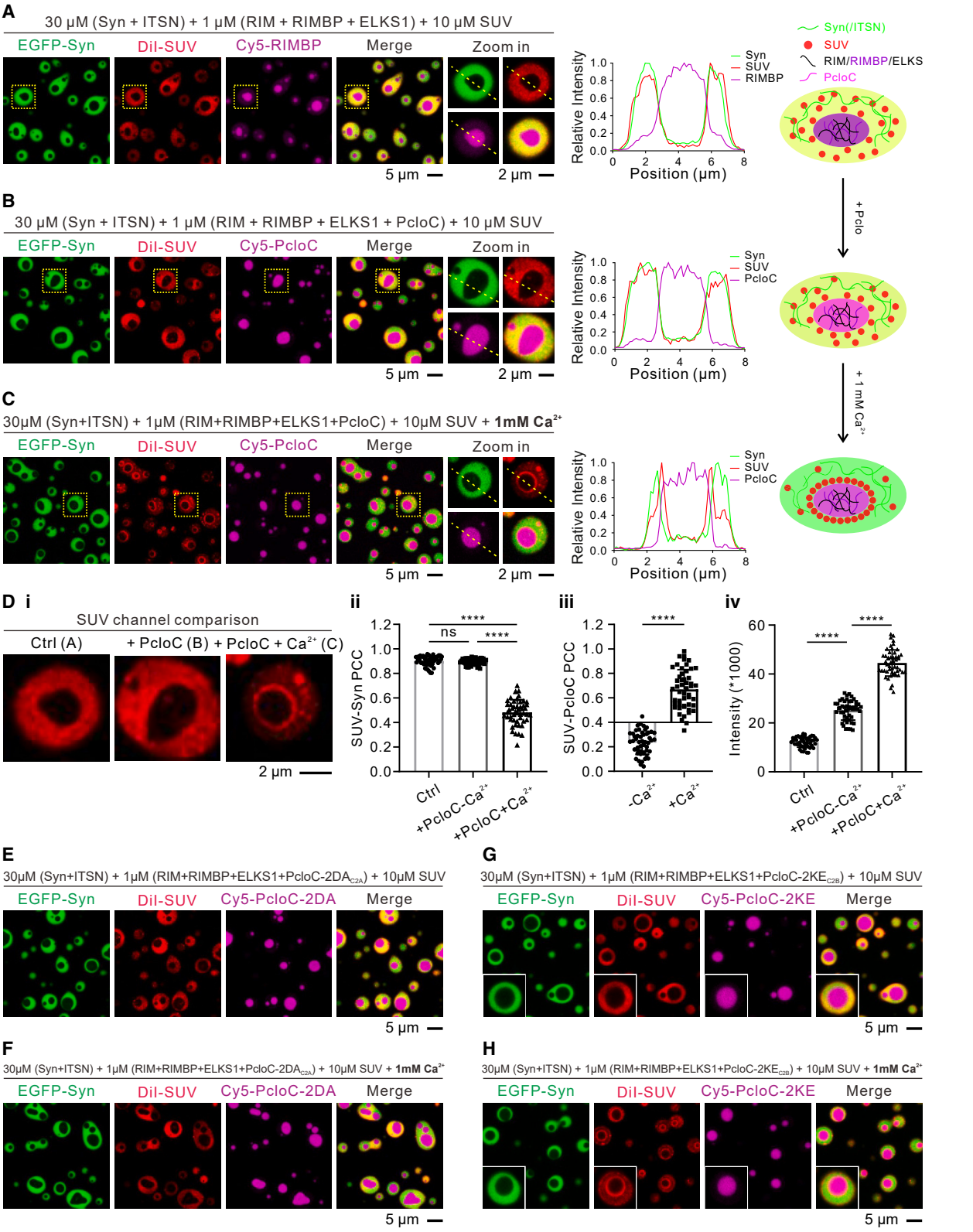

(legend on next page)

and S7G). FRAP assay showed that the fluorescence signals of TFG, either alone or when coacervated with SUVs, could rapidly recover after photobleaching (Figures 7Fi–7Fiii), indicating that TFG even when coacervated with SUV condensates is highly mobile.

We then employed the correlative light electron microscopy (CLEM) to directly visualize COPII vesicles within TFG condensates. In the stable HeLa cells expressing mCherry-TFG, we first observed punctate fluorescence signals under confocal microscopy, then obtained 80 nm thick slices at selected fluorescent loci and imaged them under transmission electron microscopy (TEM). Multiple vesicles with diameter ~60 nm could be observed within or attached at the peripheral of the electron-dense TFG condensates (Figure 7G), in line with the fluorescence imaging of co-enrichment of TFG condensates and COPII vesicles (Figure 7A). Neither latrunculin A nor nocodazole treatments affected TFG condensates formation, its coacervation with COPII vesicles, and their movements (Figure 7H), indicating that neither actin filaments nor microtubules are required/involved in the TFG-assisted short-distance COPII trafficking.

DISCUSSION

Motor-powered long-distance transport vs. phase-separation-mediated short-distance transport of cellular vesicles

Intracellular vesicular transport is vital for biomolecular trafficking as well as membrane homeostasis and thus participates in various aspects of biological processes such as anterograde ER to Golgi transport, retrograde Golgi to ER transport, trans-Golgi network transport, endocytic vesicle transport, membrane trafficking in autophagy, etc.[71,72] The best-studied vesicle transport processes are movements of vesicles along cytoskeleton tracks by molecular motors. For long-distance vesicle trafficking, molecular motors are essential, as otherwise, delivery of vesicles by diffusion to a specific cellular localization is both too slow and inefficient.[73,74] However, how vesicles are transported between localized cellular sub-compartments that are not far apart or lack of cytoskeletal tracks is totally unknown. Directional SV transport from reserve pool to the release sites in presynaptic boutons of neurons and bi-directional vesicle transport between Golgi cisternae are two prominent examples of such local, short-distance directional vesicle movements. Many other vesicles (e.g., secretory vesicles in ER and Golgi stacks, autophagic and lysosomal vesicles, etc.) may also undergo short-distance transport during their biogenesis.

In this study, we discovered that protein condensates formed via phase separation can effectively transport vesicles from one compartment to another compartment. Specifically, we found that Pclo, an abundant and elongated CC protein located specifically in presynaptic boutons, can extract SVs from the synapsin-clustered reserve pool and deposit the extracted vesicles onto the surface of the active zone condensate. This Pclo-mediated SV transport from the synapsin condensate to the active zone condensate surface is regulated by Ca^{2+}, a process consistent with synaptic stimulation-induced SV transport in living neurons.[75] Mechanistically, such Ca^{2+}-regulated directional SV transport between different protein condensates is due to different partitioning properties of SVs in these presynaptic protein condensates. For example, synapsin is one of the most abundant scaffold proteins in the presynaptic boutons,[76,77] and thus most SVs are clustered and stored by the synapsin condensate via phase separation.[25,31] Pclo can co-condensate with synapsin and SVs in the absence of Ca^{2+}. Ca^{2+} enhances the affinity between Pclo and SVs and thus causes extraction of SVs from the synapsin pool to form the Pclo/SV condensate via phase separation (Figures 1 and 2). Because Pclo specifically binds to multiple active zone proteins including ELKS1/2 and RIMBP with high affinity and specificity, Pclo can rapidly coacervate with the active zone proteins due to its higher partitioning tendency with the active zone condensate, leaving SVs coating on the surface of the active zone condensate (Figures 4 and 5). The portion of SVs that were extracted from the synapsin-clustered pool and form co-condensate with Pclo are rather transient and reminiscent of the imagined shuttling/recycling pool of SVs. The coating of SVs on the surface of the active zone requires charge-mediated interactions of SVs with active zone proteins including Pclo and RIM (Figure 2). Why SVs do not enter the active zone condensate is currently unknown, but the coating of SVs to the active zone protein densities is a well-established observation from EM experiments.[52,78] Thus, we have demonstrated, using the reconstituted presynaptic SV transport as a paradigm, that short-distance and directional vesicle transport can be achieved via phase separation of vesicles with protein condensates without involving molecular motors. Such phase-separation-mediated short-distance vesicle transport also occurs in the COPII-coated vesicle transport between ER and ERGIC (Figure 7).

Figure 6. Ca^{2+}-dependent, PcloC-mediated vesicle transport from the synapsin condensate to the active zone condensate

(A) Confocal images showing that the RIM/RIMBP/ELKS1 condensate was encapsulated by the synapsin/ITSN/SUV condensate. A dashed box was selected for zoom-in and line-scanning analyses (middle). A graphic model depicted the organization of the active zone condensate with the synapsin condensate at right.

(B and C) Representative images showing the organizations of the RIM/RIMBP/ELKS1/PcloC condensate and the synapsin/ITSN/SUV condensate in the absence (B) or presence of 1 mM Ca^{2+} (C).

(D) Quantification of images in (A)–(C). Zoom-in of the boxed images of the SUV channel in (A)–(C) (Di). PCC between SUV and synapsin (Dii), or between SUV and PcloC (Diii), and SUV coating on the surface of the RIM/RIMBP/ELKS1/PcloC condensate expressed as SUV fluorescence signal intensity as described in Figure 5D (Div).

(E and F) Representative images showing the organizations of the RIM/RIMBP/ELKS1/PcloC-2DA$_{C2A}$ condensate and the synapsin/ITSN/SUV condensate in the absence (E) or presence of 1 mM Ca^{2+} (F).

(G and H) Representative images showing the organizations of the RIM/RIMBP/ELKS1/PcloC-2KE$_{C2B}$ condensate and the synapsin/ITSN/SUV condensate in the absence (G) or presence of 1 mM Ca^{2+} (H). A zoom-in image of a droplet is shown at the lower left corner.

See also Figure S6.

Please cite this article in press as: Qiu et al., Short-distance vesicle transport via phase separation, Cell (2024), https://doi.org/10.1016/j.cell.2024.03.003

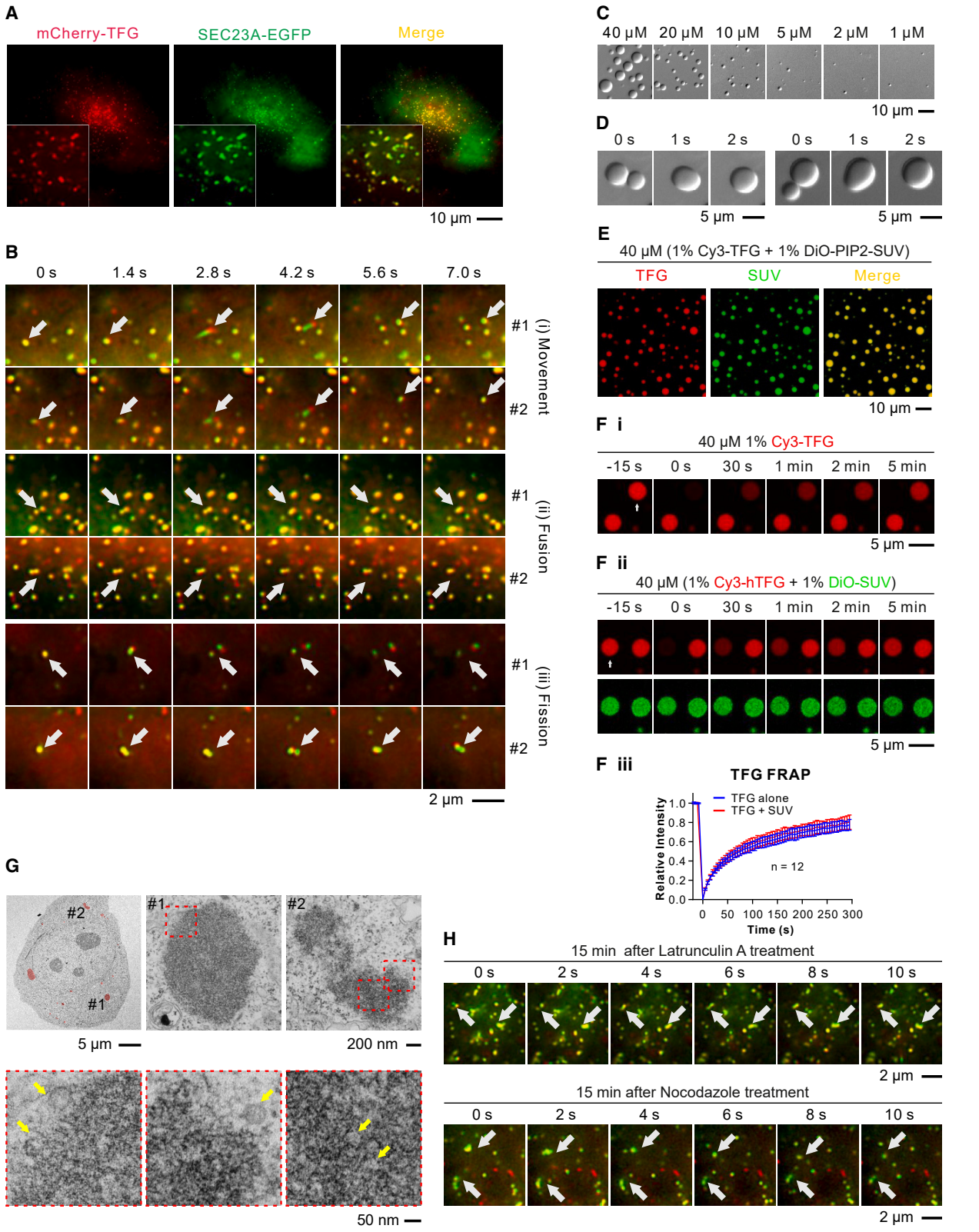

(legend on next page)

Please cite this article in press as: Qiu et al., Short-distance vesicle transport via phase separation, Cell (2024), https://doi.org/10.1016/j.cell.2024.03.003

There is a substantial body of physiological studies supporting our reconstitution-based discoveries. Pclo was identified from rat brain synaptic preparations and localized at the presynaptic active zone.[36,79] Multicolor three-dimensional stochastic optical reconstruction microscopy studies showed that the giant Pclo adopts elongated conformation with its C-terminal part contacting active zone and the N-terminal end connecting the reserve pool in presynaptic boutons.[80] An immunogold electron microscopy study showed that Pclo forms compact clusters that are ~35–80 nm away from the presynaptic plasma membrane.[52] These imaging results strongly suggest Pclo, likely together with Bassoon, may function as linkers connecting reserve pool SVs and docked SVs at the active zone, as we have shown in Figures 5 and 6. Importantly, it has been shown that genetic removal of Pclo and/or Bassoon, both in the central nervous system and in ribbon synapse from hair cells or photoreceptors, results in defects of moving SVs from reserve pool to the active zone to replenish the docking sites vacated by fused vesicles when synapses are repeatedly stimulated.[39,43,81] These genetic studies suggest that Pclo functions in moving SVs from reserve pool to the docked pool on the active zone in response to synaptic stimulations. The findings presented in this study provide a molecular mechanism showing that Pclo, in response to Ca^{2+}, can move SVs from reserve pool to the docked pool via modulating vesicle partitioning in different protein condensates formed via phase separation.

General implications of phase-separation-directed short-distance vesicle transport

We also provided some evidence that COPII vesicle trafficking from ER to ERGIC also involves protein phase separation. We show that TFG condensate coacervation with COPII vesicles and regulates COPII vesicle trafficking from ER to ERGIC in a cytoskeleton-independent manner (Figure 7), although much more investigations are required to understand the underlying molecular mechanism. It is known that vesicle transport between Golgi cisternae requires a family of proteins called golgins.[82–84] We note with interest that, analogous to Pclo and ELKS, golgins are also elongated CC proteins that can interact with and capture vesicles.[85,86] Golgins have also been shown to form condensates via phase separation.[87–89] It will be interesting to investigate whether golgins, possibly via working with other intra-Golgi trafficking proteins, may facilitate vesicle transport in Golgi apparatus. We further note that many peripheral membrane-interacting proteins involved in various vesicle biogenesis processes, such as FIP200, NDP52, and Atg11 in autophagy[90–93]; flotillins, EEA1, and p180 in endosome and lysosome biogenesis[94–96]; EPS15 and Ede1 in endocytosis,[97,98] are also large CC-containing proteins akin to Pclo, ELKS, and TFG. Phase separation is known to be involved in the biogenesis of these vesicles. Thus, it is possible that phase separation may be a general mechanism in the directed, short-distance vesicle transport in cells.

Limitations of the study

A key limitation of this study is that we used *in vitro* reconstitution approaches to show phase-separation-mediated shuttling of vesicles from the reserve pool protein condensate to the active zone protein condensate. Direct synaptic biology investigations to connect this *in vitro* biochemical study with synaptic functions in living neurons are needed in the future. Additionally, it should be noted that the concentration Ca^{2+} used in the *in vitro* SV transport experiments is higher than the physiological Ca^{2+} concentrations in presynaptic boutons. Another limitation is that, due to the extremely long length of Pclo and the resulting challenges in purifying the full-length protein, the conserved C-terminal part of Pclo was used in our reconstitution study. The N-terminal part of Pclo may modify the phase separation property of the protein with vesicles. Finally, this study has not addressed whether lipids from the presynaptic plasma membranes may also contribute to the Ca^{2+}-dependent short-distance vesicle transport.

STAR★METHODS

Detailed methods are provided in the online version of this paper and include the following:

- KEY RESOURCES TABLE
- RESOURCE AVAILABILITY
  - Lead contact
  - Materials availability
  - Data and code availability
- EXPERIMENTAL MODEL AND STUDY PARTICIPANT DETAILS
  - Bacterial strain
  - Cell line
- METHOD DETAILS
  - Genes and plasmids
  - Protein expression and purification
  - Fluorophore labelling of proteins

Figure 7. TFG condensates mediate early secretion COPII vesicle organization and trafficking

(A) Representative images of COS7 cells stably expressing mCherry-TFG and transiently transfected with SEC23A-EGFP. Insert is a 4× zoom-in image.

(B) TFG/SEC23A condensates are highly mobile. Two typical examples of fast co-movements (Bi), fusion (Bii), and fission (Biii) events are represented.

(C) Purified TFG undergoes phase separation *in vitro*. Protein concentrations are denoted. Buffer condition: 100 HBS supplemented with 3% PEG8,000.

(D) Two examples of time-lapse images showing rapid fusion of TFG droplets upon contacting each other.

(E) TFG condensates acervate with PIP2-containing SUVs.

(F) FRAP of TFG in the absence (Fi) or presence (Fii) of SUV. The recovery curves have no substantial difference between the two conditions (Fiii) based on unpaired t test analysis.

(G) Representative correlative light electron microscopy (CLEM) images of HeLa cells stably expressing mCherry-TFG showing clustering of vesicles within the TFG condensates. Pseudo-colored fluorescence image was merged with the EM image to mark the slice loci labeled as #1 and #2.

(H) Neither disassembly of actin filaments by latrunculin A nor disruption of microtubules by nocodazole affects TFG condensates formation and coacervation of TFG condensates with COPII vesicles.

See also Figure S7.

- Small Unilamellar Vesicle (SUV) preparation
- Phase separation assays: sample preparation and imaging
- Fluorescence recovery after photobleaching (FRAP) assay
- Liposome binding assay
- Synaptic vesicle (SV) purification, labeling, and trypsin digestion
- Isothermal titration calorimetry (ITC) assay
- Size exclusion chromatography coupled with multiangle light scattering (SEC-MALS) assay
- Protein crystallization and structure determination
- Generation of stable cell lines expressing mCherry-TFG or EGFP-TFG
- Multi-modal SIM (multi-SIM) live cell imaging
- Correlative light and electron microscopy

● QUANTIFICATION AND STATISTICAL ANALYSIS

SUPPLEMENTAL INFORMATION

Supplemental information can be found online at https://doi.org/10.1016/j.cell.2024.03.003.

ACKNOWLEDGMENTS

We thank the BL19U1 beamline at the National Facility for Protein Science Shanghai for X-ray beam time, Dr. Reinhard Jahn for his insightful comments on the manuscript, and Dr. Johann Helmut Brandstätter for providing cDNA clones of Pclo fragments used in this study. This work was supported by grants from the National Natural Science Foundation of China (82188101), the Ministry of Science and Technology of China (2019YFA0508402), the Research Grant Council of Hong Kong (16104518 and 16101419), the Shenzhen Bay Laboratory (S201101002), the Shenzhen Talent Program (KQTD20210811090115021), the Shenzhen Science and Technology Basic Research Program (JCYJ20220818100215033), the Shenzhen Key Laboratory (ZDSYS20220402111000001), and the Guangdong Innovative and Entrepreneurial Research Team Program (2021ZT09Y104) to M.Z. X.W. receives a postdoctoral fellowship from the Research Grant Council of Hong Kong (HKUST PDFS2122-6S04).

AUTHOR CONTRIBUTIONS

H.Q. and X.W. performed all phase-separation-related experiments. X.M. performed the cell biology study of TFG. Q.C. solved the structure of the ELKS1/Pclo complex. S.L. performed the CLEM experiment on TFG. M.G. purified rat SVs. All authors analyzed the data. X.W., H.Q., and M.Z. designed research. L.G., H.Z., and M.Z. supervised the research. X.W. and M.Z. drafted and all authors commented the paper. M.Z. coordinated the study.

DECLARATION OF INTERESTS

The authors declare no competing interests.

Received: January 31, 2023
Revised: January 17, 2024
Accepted: March 2, 2024
Published: March 28, 2024

REFERENCES

1. Vale, R.D. (1987). Intracellular transport using microtubule-based motors. Annu. Rev. Cell Biol. *3*, 347–378. https://doi.org/10.1146/annurev.cb.03.110187.002023.
2. Barlan, K., and Gelfand, V.I. (2017). Microtubule-based transport and the distribution, tethering, and organization of organelles. Cold Spring Harbor Perspect. Biol. *9*, a025817. https://doi.org/10.1101/cshperspect.a025817.
3. Miller, E.A., and Schekman, R. (2013). COPII - a flexible vesicle formation system. Curr. Opin. Cell Biol. *25*, 420–427. https://doi.org/10.1016/j.ceb.2013.04.005.
4. S Mogre, S.S., Brown, A.I., and Koslover, E.F. (2020). Getting around the cell: physical transport in the intracellular world. Phys. Biol. *17*, 061003. https://doi.org/10.1088/1478-3975/aba5e5.
5. Vale, R.D., and Milligan, R.A. (2000). The way things move: looking under the hood of molecular motor proteins. Science *288*, 88–95. https://doi.org/10.1126/science.288.5463.88.
6. Vale, R.D. (2003). The molecular motor toolbox for intracellular transport. Cell *112*, 467–480. https://doi.org/10.1016/s0092-8674(03)00111-9.
7. Kamal, A., and Goldstein, L.S. (2000). Connecting vesicle transport to the cytoskeleton. Curr. Opin. Cell Biol. *12*, 503–508. https://doi.org/10.1016/s0955-0674(00)00123-x.
8. Lee, M.C., Miller, E.A., Goldberg, J., Orci, L., and Schekman, R. (2004). Bi-directional protein transport between the ER and Golgi. Annu. Rev. Cell Dev. Biol. *20*, 87–123. https://doi.org/10.1146/annurev.cellbio.20.010403.105307.
9. Gomez-Navarro, N., and Miller, E. (2016). Protein sorting at the ER-Golgi interface. J. Cell Biol. *215*, 769–778. https://doi.org/10.1083/jcb.201610031.
10. Mochida, S. (2020). Neurotransmitter release site replenishment and presynaptic plasticity. Int. J. Mol. Sci. *22*, 327. https://doi.org/10.3390/ijms22010327.
11. Südhof, T.C. (2012). Calcium control of neurotransmitter release. Cold Spring Harbor Perspect. Biol. *4*, a011353. https://doi.org/10.1101/cshperspect.a011353.
12. Chanaday, N.L., Cousin, M.A., Milosevic, I., Watanabe, S., and Morgan, J.R. (2019). The synaptic vesicle cycle revisited: new insights into the modes and mechanisms. J. Neurosci. *39*, 8209–8216. https://doi.org/10.1523/JNEUROSCI.1158-19.2019.
13. Sudhof, T.C. (2004). The synaptic vesicle cycle. Annu. Rev. Neurosci. *27*, 509–547. https://doi.org/10.1146/annurev.neuro.26.041002.131412.
14. Brown, A. (2003). Axonal transport of membranous and nonmembranous cargoes: a unified perspective. J. Cell Biol. *160*, 817–821. https://doi.org/10.1083/jcb.200212017.
15. Guedes-Dias, P., and Holzbaur, E.L.F. (2019). Axonal transport: driving synaptic function. Science *366*, eaaw9997. https://doi.org/10.1126/science.aaw9997.
16. Pieribone, V.A., Shupliakov, O., Brodin, L., Hilfiker-Rothenfluh, S., Czernik, A.J., and Greengard, P. (1995). Distinct pools of synaptic vesicles in neurotransmitter release. Nature *375*, 493–497. https://doi.org/10.1038/375493a0.
17. Rizzoli, S.O., and Betz, W.J. (2005). Synaptic vesicle pools. Nat. Rev. Neurosci. *6*, 57–69. https://doi.org/10.1038/nrn1583.
18. Siksou, L., Rostaing, P., Lechaire, J.P., Boudier, T., Ohtsuka, T., Fejtová, A., Kao, H.T., Greengard, P., Gundelfinger, E.D., Triller, A., and Marty, S. (2007). Three-dimensional architecture of presynaptic terminal cytomatrix. J. Neurosci. *27*, 6868–6877. https://doi.org/10.1523/JNEUROSCI.1773-07.2007.
19. Alabi, A.A., and Tsien, R.W. (2012). Synaptic vesicle pools and dynamics. Cold Spring Harb. Perspect. Biol. *4*, a013680. https://doi.org/10.1101/cshperspect.a013680.
20. Tokuoka, H., and Goda, Y. (2006). Myosin light chain kinase is not a regulator of synaptic vesicle trafficking during repetitive exocytosis in cultured hippocampal neurons. J. Neurosci. *26*, 11606–11614. https://doi.org/10.1523/JNEUROSCI.3400-06.2006.
21. Fernández-Busnadiego, R., Zuber, B., Maurer, U.E., Cyrklaff, M., Baumeister, W., and Lucic, V. (2010). Quantitative analysis of the native

presynaptic cytomatrix by cryoelectron tomography. J. Cell Biol. *188*, 145–156. https://doi.org/10.1083/jcb.200908082.

22. Nelson, J.C., Stavoe, A.K., and Colón-Ramos, D.A. (2013). The actin cytoskeleton in presynaptic assembly. Cell Adh. Migr. *7*, 379–387. https://doi.org/10.4161/cam.24803.
23. Chen, X., Wu, X., Wu, H., and Zhang, M. (2020). Phase separation at the synapse. Nat. Neurosci. *23*, 301–310. https://doi.org/10.1038/s41593-019-0579-9.
24. Wu, X., Cai, Q., Feng, Z., and Zhang, M. (2020). Liquid-liquid phase separation in neuronal development and synaptic signaling. Dev. Cell *55*, 18–29. https://doi.org/10.1016/j.devcel.2020.06.012.
25. Milovanovic, D., Wu, Y., Bian, X., and De Camilli, P. (2018). A liquid phase of synapsin and lipid vesicles. Science *361*, 604–607. https://doi.org/10.1126/science.aat5671.
26. Wu, X., Cai, Q., Shen, Z., Chen, X., Zeng, M., Du, S., and Zhang, M. (2019). RIM and RIM-BP form presynaptic active-zone-like condensates via phase separation. Mol. Cell *73*, 971–984.e5. https://doi.org/10.1016/j.molcel.2018.12.007.
27. McDonald, N.A., Fetter, R.D., and Shen, K. (2020). Assembly of synaptic active zones requires phase separation of scaffold molecules. Nature *588*, 454–458. https://doi.org/10.1038/s41586-020-2942-0.
28. Emperador-Melero, J., Wong, M.Y., Wang, S.S.H., de Nola, G., Nyitrai, H., Kirchhausen, T., and Kaeser, P.S. (2021). PKC-phosphorylation of liprin-alpha3 triggers phase separation and controls presynaptic active zone structure. Nat. Commun. *12*, 3057. https://doi.org/10.1038/s41467-021-23116-w.
29. Wu, X., Ganzella, M., Zhou, J., Zhu, S., Jahn, R., and Zhang, M. (2021). Vesicle tethering on the surface of phase-separated active zone condensates. Mol. Cell *81*, 13–24.e7. https://doi.org/10.1016/j.molcel.2020.10.029.
30. Park, D., Wu, Y., Lee, S.E., Kim, G., Jeong, S., Milovanovic, D., De Camilli, P., and Chang, S. (2021). Cooperative function of synaptophysin and synapsin in the generation of synaptic vesicle-like clusters in non-neuronal cells. Nat. Commun. *12*, 263. https://doi.org/10.1038/s41467-020-20462-z.
31. Pechstein, A., Tomilin, N., Fredrich, K., Vorontsova, O., Sopova, E., Evergren, E., Haucke, V., Brodin, L., and Shupliakov, O. (2020). Vesicle clustering in a living synapse depends on a synapsin region that mediates phase separation. Cell Rep. *30*, 2594–2602.e3. https://doi.org/10.1016/j.celrep.2020.01.092.
32. Liang, M., Jin, G., Xie, X., Zhang, W., Li, K., Niu, F., Yu, C., and Wei, Z. (2021). Oligomerized liprin-alpha promotes phase separation of ELKS for compartmentalization of presynaptic active zone proteins. Cell Rep. *34*, 108901. https://doi.org/10.1016/j.celrep.2021.108901.
33. Feng, Z., Wu, X., and Zhang, M. (2021). Presynaptic bouton compartmentalization and postsynaptic density-mediated glutamate receptor clustering via phase separation. Neuropharmacology *193*, 108622. https://doi.org/10.1016/j.neuropharm.2021.108622.
34. Wu, X., Qiu, H., and Zhang, M. (2023). Interactions between membraneless condensates and membranous organelles at the presynapse: A phase separation View of synaptic vesicle cycle. J. Mol. Biol. *435*, 167629. https://doi.org/10.1016/j.jmb.2022.167629.
35. Jin, Y., and Garner, C.C. (2008). Molecular mechanisms of presynaptic differentiation. Annu. Rev. Cell Dev. Biol. *24*, 237–262. https://doi.org/10.1146/annurev.cellbio.23.090506.123417.
36. Gundelfinger, E.D., Reissner, C., and Garner, C.C. (2015). Role of bassoon and Piccolo in assembly and molecular organization of the active zone. Front. Synaptic Neurosci. *7*, 19. https://doi.org/10.3389/fnsyn.2015.00019.
37. Südhof, T.C. (2012). The presynaptic active zone. Neuron *75*, 11–25. https://doi.org/10.1016/j.neuron.2012.06.012.
38. Emperador-Melero, J., and Kaeser, P.S. (2020). Assembly of the presynaptic active zone. Curr. Opin. Neurobiol. *63*, 95–103. https://doi.org/10.1016/j.conb.2020.03.008.
39. Hallermann, S., Fejtova, A., Schmidt, H., Weyhersmüller, A., Silver, R.A., Gundelfinger, E.D., and Eilers, J. (2010). Bassoon speeds vesicle reloading at a central excitatory synapse. Neuron *68*, 710–723. https://doi.org/10.1016/j.neuron.2010.10.026.
40. Mukherjee, K., Yang, X., Gerber, S.H., Kwon, H.B., Ho, A., Castillo, P.E., Liu, X., and Südhof, T.C. (2010). Piccolo and bassoon maintain synaptic vesicle clustering without directly participating in vesicle exocytosis. Proc. Natl. Acad. Sci. USA *107*, 6504–6509. https://doi.org/10.1073/pnas.1002307107.
41. Ackermann, F., Schink, K.O., Bruns, C., Izsvák, Z., Hamra, F.K., Rosenmund, C., and Garner, C.C. (2019). Critical role for Piccolo in synaptic vesicle retrieval. eLife *8*, e46629. https://doi.org/10.7554/eLife.46629.
42. Waites, C.L., Leal-Ortiz, S.A., Okerlund, N., Dalke, H., Fejtova, A., Altrock, W.D., Gundelfinger, E.D., and Garner, C.C. (2013). Bassoon and Piccolo maintain synapse integrity by regulating protein ubiquitination and degradation. EMBO J. *32*, 954–969. https://doi.org/10.1038/emboj.2013.27.
43. Butola, T., Wichmann, C., and Moser, T. (2017). Piccolo promotes vesicle replenishment at a fast central auditory synapse. Front. Synaptic Neurosci. *9*, 14. https://doi.org/10.3389/fnsyn.2017.00014.
44. Rosahl, T.W., Spillane, D., Missler, M., Herz, J., Selig, D.K., Wolff, J.R., Hammer, R.E., Malenka, R.C., and Südhof, T.C. (1995). Essential functions of synapsins I and II in synaptic vesicle regulation. Nature *375*, 488–493. https://doi.org/10.1038/375488a0.
45. Gitler, D., Takagishi, Y., Feng, J., Ren, Y., Rodriguiz, R.M., Wetsel, W.C., Greengard, P., and Augustine, G.J. (2004). Different presynaptic roles of synapsins at excitatory and inhibitory synapses. J. Neurosci. *24*, 11368–11380. https://doi.org/10.1523/JNEUROSCI.3795-04.2004.
46. Wang, S.S.H., Held, R.G., Wong, M.Y., Liu, C., Karakhanyan, A., and Kaeser, P.S. (2016). Fusion competent synaptic vesicles persist upon active zone disruption and loss of vesicle docking. Neuron *91*, 777–791. https://doi.org/10.1016/j.neuron.2016.07.005.
47. Acuna, C., Liu, X., and Südhof, T.C. (2016). How to make an active zone: unexpected universal functional redundancy between RIMs and RIM-BPs. Neuron *91*, 792–807. https://doi.org/10.1016/j.neuron.2016.07.042.
48. Kaeser, P.S., and Regehr, W.G. (2017). The readily releasable pool of synaptic vesicles. Curr. Opin. Neurobiol. *43*, 63–70. https://doi.org/10.1016/j.conb.2016.12.012.
49. Fenster, S.D., Chung, W.J., Zhai, R., Cases-Langhoff, C., Voss, B., Garner, A.M., Kaempf, U., Kindler, S., Gundelfinger, E.D., and Garner, C.C. (2000). Piccolo, a presynaptic zinc finger protein structurally related to bassoon. Neuron *25*, 203–214. https://doi.org/10.1016/s0896-6273(00)80883-1.
50. Gerber, S.H., Garcia, J., Rizo, J., and Südhof, T.C. (2001). An unusual C(2)-domain in the active-zone protein piccolo: implications for Ca(2+) regulation of neurotransmitter release. EMBO J. *20*, 1605–1619. https://doi.org/10.1093/emboj/20.7.1605.
51. Wang, X., Hu, B., Zieba, A., Neumann, N.G., Kasper-Sonnenberg, M., Honsbein, A., Hultqvist, G., Conze, T., Witt, W., Limbach, C., et al. (2009). A protein interaction node at the neurotransmitter release site: domains of Aczonin/Piccolo, Bassoon, CAST, and rim converge on the N-terminal domain of Munc13-1. J. Neurosci. *29*, 12584–12596. https://doi.org/10.1523/JNEUROSCI.1255-09.2009.
52. Limbach, C., Laue, M.M., Wang, X., Hu, B., Thiede, N., Hultqvist, G., and Kilimann, M.W. (2011). Molecular in situ topology of Aczonin/Piccolo and associated proteins at the mammalian neurotransmitter release site. Proc. Natl. Acad. Sci. USA *108*, E392–E401. https://doi.org/10.1073/pnas.1101707108.

53. Schneggenburger, R., and Neher, E. (2000). Intracellular calcium dependence of transmitter release rates at a fast central synapse. Nature *406*, 889–893. https://doi.org/10.1038/35022702.

54. Neher, E., and Sakaba, T. (2008). Multiple roles of calcium ions in the regulation of neurotransmitter release. Neuron *59*, 861–872. https://doi.org/10.1016/j.neuron.2008.08.019.

55. Takamori, S., Holt, M., Stenius, K., Lemke, E.A., Grønborg, M., Riedel, D., Urlaub, H., Schenck, S., Brügger, B., Ringler, P., et al. (2006). Molecular anatomy of a trafficking organelle. Cell *127*, 831–846. https://doi.org/10.1016/j.cell.2006.10.030.

56. Garcia, J., Gerber, S.H., Sugita, S., Südhof, T.C., and Rizo, J. (2004). A conformational switch in the Piccolo C2A domain regulated by alternative splicing. Nat. Struct. Mol. Biol. *11*, 45–53. https://doi.org/10.1038/nsmb707.

57. Guan, R., Dai, H., Tomchick, D.R., Dulubova, I., Machius, M., Südhof, T.C., and Rizo, J. (2007). Crystal structure of the RIM1alpha C2B domain at 1.7 A resolution. Biochemistry *46*, 8988–8998. https://doi.org/10.1021/bi700698a.

58. de Jong, A.P.H., Roggero, C.M., Ho, M.R., Wong, M.Y., Brautigam, C.A., Rizo, J., and Kaeser, P.S. (2018). RIM C2B domains target presynaptic active zone functions to PIP2-containing membranes. Neuron *98*, 335–349.e7. https://doi.org/10.1016/j.neuron.2018.03.011.

59. Davydova, D., Marini, C., King, C., Klueva, J., Bischof, F., Romorini, S., Montenegro-Venegas, C., Heine, M., Schneider, R., Schröder, M.S., et al. (2014). Bassoon specifically controls presynaptic P/Q-type Ca(2+) channels via RIM-binding protein. Neuron *82*, 181–194. https://doi.org/10.1016/j.neuron.2014.02.012.

60. Takao-Rikitsu, E., Mochida, S., Inoue, E., Deguchi-Tawarada, M., Inoue, M., Ohtsuka, T., and Takai, Y. (2004). Physical and functional interaction of the active zone proteins, CAST, RIM1, and Bassoon, in neurotransmitter release. J. Cell Biol. *164*, 301–311. https://doi.org/10.1083/jcb.200307101.

61. Maas, C., Torres, V.I., Altrock, W.D., Leal-Ortiz, S., Wagh, D., Terry-Lorenzo, R.T., Fejtova, A., Gundelfinger, E.D., Ziv, N.E., and Garner, C.C. (2012). Formation of Golgi-derived active zone precursor vesicles. J. Neurosci. *32*, 11095–11108. https://doi.org/10.1523/JNEUROSCI.0195-12.2012.

62. Held, R.G., and Kaeser, P.S. (2018). ELKS active zone proteins as multitasking scaffolds for secretion. Open Biol. *8*, 170258. https://doi.org/10.1098/rsob.170258.

63. Nyitrai, H., Wang, S.S.H., and Kaeser, P.S. (2020). ELKS1 captures Rab6-marked vesicular cargo in presynaptic nerve terminals. Cell Rep. *31*, 107712. https://doi.org/10.1016/j.celrep.2020.107712.

64. Zeuschner, D., Geerts, W.J., van Donselaar, E., Humbel, B.M., Slot, J.W., Koster, A.J., and Klumperman, J. (2006). Immuno-electron tomography of ER exit sites reveals the existence of free COPII-coated transport carriers. Nat. Cell Biol. *8*, 377–383. https://doi.org/10.1038/ncb1371.

65. Johnson, A., Bhattacharya, N., Hanna, M., Pennington, J.G., Schuh, A.L., Wang, L., Otegui, M.S., Stagg, S.M., and Audhya, A. (2015). TFG clusters COPII-coated transport carriers and promotes early secretory pathway organization. EMBO J. *34*, 811–827. https://doi.org/10.15252/embj.201489032.

66. Witte, K., Schuh, A.L., Hegermann, J., Sarkeshik, A., Mayers, J.R., Schwarze, K., Yates, J.R., 3rd, Eimer, S., and Audhya, A. (2011). TFG-1 function in protein secretion and oncogenesis. Nat. Cell Biol. *13*, 550–558. https://doi.org/10.1038/ncb2225.

67. Hanna, M.G.t., Block, S., Frankel, E.B., Hou, F., Johnson, A., Yuan, L., Knight, G., Moresco, J.J., Yates, J.R., 3rd, Ashton, R., et al. (2017). TFG facilitates outer coat disassembly on COPII transport carriers to promote tethering and fusion with ER-Golgi intermediate compartments. Proc. Natl. Acad. Sci. USA *114*, E7707–E7716. https://doi.org/10.1073/pnas.1709120114.

68. Simpson, J.C., Joggerst, B., Laketa, V., Verissimo, F., Cetin, C., Erfle, H., Bexiga, M.G., Singan, V.R., Hériché, J.K., Neumann, B., et al. (2012). Genome-wide RNAi screening identifies human proteins with a regulatory function in the early secretory pathway. Nat. Cell Biol. *14*, 764–774. https://doi.org/10.1038/ncb2510.

69. Feng, Z., Jia, B., and Zhang, M. (2021). Liquid-liquid phase separation in biology: specific stoichiometric molecular interactions vs promiscuous interactions mediated by disordered sequences. Biochemistry *60*, 2397–2406. https://doi.org/10.1021/acs.biochem.1c00376.

70. Shen, Z., Jia, B., Xu, Y., Wessén, J., Pal, T., Chan, H.S., Du, S., and Zhang, M. (2023). Biological condensates form percolated networks with molecular motion properties distinctly different from dilute solutions. eLife *12*, e81907. https://doi.org/10.7554/eLife.81907.

71. Cui, L., Li, H., Xi, Y., Hu, Q., Liu, H., Fan, J., Xiang, Y., Zhang, X., Shui, W., and Lai, Y. (2022). Vesicle trafficking and vesicle fusion: mechanisms, biological functions, and their implications for potential disease therapy. Mol. Biomed. *3*, 29. https://doi.org/10.1186/s43556-022-00090-3.

72. Bonifacino, J.S., and Glick, B.S. (2004). The mechanisms of vesicle budding and fusion. Cell *116*, 153–166. https://doi.org/10.1016/s0092-8674(03)01079-1.

73. De Vos, K.J., Grierson, A.J., Ackerley, S., and Miller, C.C. (2008). Role of axonal transport in neurodegenerative diseases. Annu. Rev. Neurosci. *31*, 151–173. https://doi.org/10.1146/annurev.neuro.31.061307.090711.

74. Millecamps, S., and Julien, J.P. (2013). Axonal transport deficits and neurodegenerative diseases. Nat. Rev. Neurosci. *14*, 161–176. https://doi.org/10.1038/nrn3380.

75. Schnee, M.E., Santos-Sacchi, J., Castellano-Muñoz, M., Kong, J.H., and Ricci, A.J. (2011). Calcium-dependent synaptic vesicle trafficking underlies indefatigable release at the hair cell afferent fiber synapse. Neuron *70*, 326–338. https://doi.org/10.1016/j.neuron.2011.01.031.

76. Wilhelm, B.G., Mandad, S., Truckenbrodt, S., Kröhnert, K., Schäfer, C., Rammner, B., Koo, S.J., Claßen, G.A., Krauss, M., Haucke, V., et al. (2014). Composition of isolated synaptic boutons reveals the amounts of vesicle trafficking proteins. Science *344*, 1023–1028. https://doi.org/10.1126/science.1252884.

77. Cesca, F., Baldelli, P., Valtorta, F., and Benfenati, F. (2010). The synapsins: key actors of synapse function and plasticity. Prog. Neurobiol. *91*, 313–348. https://doi.org/10.1016/j.pneurobio.2010.04.006.

78. Imig, C., Min, S.W., Krinner, S., Arancillo, M., Rosenmund, C., Südhof, T.C., Rhee, J., Brose, N., and Cooper, B.H. (2014). The morphological and molecular nature of synaptic vesicle priming at presynaptic active zones. Neuron *84*, 416–431. https://doi.org/10.1016/j.neuron.2014.10.009.

79. Langnaese, K., Seidenbecher, C., Wex, H., Seidel, B., Hartung, K., Appeltauer, U., Garner, A., Voss, B., Mueller, B., Garner, C.C., and Gundelfinger, E.D. (1996). Protein components of a rat brain synaptic junctional protein preparation. Brain Res. Mol. Brain Res. *42*, 118–122. https://doi.org/10.1016/s0169-328x(96)00147-7.

80. Dani, A., Huang, B., Bergan, J., Dulac, C., and Zhuang, X. (2010). Superresolution imaging of chemical synapses in the brain. Neuron *68*, 843–856. https://doi.org/10.1016/j.neuron.2010.11.021.

81. Parthier, D., Kuner, T., and Körber, C. (2018). The presynaptic scaffolding protein Piccolo organizes the readily releasable pool at the calyx of Held. J. Physiol. *596*, 1485–1499. https://doi.org/10.1113/JP274885.

82. Yu, I.M., and Hughson, F.M. (2010). Tethering factors as organizers of intracellular vesicular traffic. Annu. Rev. Cell Dev. Biol. *26*, 137–156. https://doi.org/10.1146/annurev.cellbio.042308.113327.

83. Malsam, J., Satoh, A., Pelletier, L., and Warren, G. (2005). Golgin tethers define subpopulations of COPI vesicles. Science *307*, 1095–1098. https://doi.org/10.1126/science.1108061.

84. Muschalik, N., and Munro, S. (2018). Golgins. Curr. Biol. *28*, R374–R376. https://doi.org/10.1016/j.cub.2018.01.006.

85. Munro, S. (2011). The golgin coiled-coil proteins of the Golgi apparatus. Cold Spring Harbor Perspect. Biol. *3*, a005256. https://doi.org/10.1101/cshperspect.a005256.

86. Gillingham, A.K., and Munro, S. (2016). Finding the Golgi: golgin coiled-coil proteins show the way. Trends Cell Biol. *26*, 399–408. https://doi.org/10.1016/j.tcb.2016.02.005.

87. Rebane, A.A., Ziltener, P., LaMonica, L.C., Bauer, A.H., Zheng, H., López-Montero, I., Pincet, F., Rothman, J.E., and Ernst, A.M. (2020). Liquid-liquid phase separation of the Golgi matrix protein GM130. FEBS Lett. *594*, 1132–1144. https://doi.org/10.1002/1873-3468.13715.

88. Rothman, J.E. (2019). Jim's View: is the Golgi stack a phase-separated liquid crystal? FEBS Lett. *593*, 2701–2705. https://doi.org/10.1002/1873-3468.13609.

89. Ziltener, P., Rebane, A.A., Graham, M., Ernst, A.M., and Rothman, J.E. (2020). The golgin family exhibits a propensity to form condensates in living cells. FEBS Lett. *594*, 3086–3094. https://doi.org/10.1002/1873-3468.13884.

90. Yamasaki, A., Alam, J.M., Noshiro, D., Hirata, E., Fujioka, Y., Suzuki, K., Ohsumi, Y., and Noda, N.N. (2020). Liquidity is a critical determinant for selective autophagy of protein condensates. Mol. Cell *77*, 1163–1175.e9. https://doi.org/10.1016/j.molcel.2019.12.026.

91. Zheng, Q., Chen, Y., Chen, D., Zhao, H., Feng, Y., Meng, Q., Zhao, Y., and Zhang, H. (2022). Calcium transients on the ER surface trigger liquid-liquid phase separation of FIP200 to specify autophagosome initiation sites. Cell *185*, 4082–4098.e22. https://doi.org/10.1016/j.cell.2022.09.001.

92. Noda, N.N., Wang, Z., and Zhang, H. (2020). Liquid-liquid phase separation in autophagy. J. Cell Biol. *219*, e202004062. https://doi.org/10.1083/jcb.202004062.

93. Turco, E., Savova, A., Gere, F., Ferrari, L., Romanov, J., Schuschnig, M., and Martens, S. (2021). Reconstitution defines the roles of p62, NBR1 and TAX1BP1 in ubiquitin condensate formation and autophagy initiation. Nat. Commun. *12*, 5212. https://doi.org/10.1038/s41467-021-25572-w.

94. Kwiatkowska, K., Matveichuk, O.V., Fronk, J., and Ciesielska, A. (2020). Flotillins: at the intersection of protein S-palmitoylation and lipid-mediated signaling. Int. J. Mol. Sci. *21*, 2283. https://doi.org/10.3390/ijms21072283.

95. Özkan, N., Koppers, M., van Soest, I., van Harten, A., Jurriens, D., Liv, N., Klumperman, J., Kapitein, L.C., Hoogenraad, C.C., and Farías, G.G. (2021). ER – lysosome contacts at a pre-axonal region regulate axonal lysosome availability. Nat. Commun. *12*, 4493. https://doi.org/10.1038/s41467-021-24713-5.

96. Kümmel, D., and Ungermann, C. (2014). Principles of membrane tethering and fusion in endosome and lysosome biogenesis. Curr. Opin. Cell Biol. *29*, 61–66. https://doi.org/10.1016/j.ceb.2014.04.007.

97. Day, K.J., Kago, G., Wang, L., Richter, J.B., Hayden, C.C., Lafer, E.M., and Stachowiak, J.C. (2021). Liquid-like protein interactions catalyse assembly of endocytic vesicles. Nat. Cell Biol. *23*, 366–376. https://doi.org/10.1038/s41556-021-00646-5.

98. Kozak, M., and Kaksonen, M. (2022). Condensation of Ede1 promotes the initiation of endocytosis. eLife *11*, e72865. https://doi.org/10.7554/eLife.72865.

99. Rodríguez, D.D., Grosse, C., Himmel, S., González, C., de Ilarduya, I.M., Becker, S., Sheldrick, G.M., and Usón, I. (2009). Crystallographic ab initio protein structure solution below atomic resolution. Nat. Methods *6*, 651–653. https://doi.org/10.1038/nmeth.1365.

100. Emsley, P., Lohkamp, B., Scott, W.G., and Cowtan, K. (2010). Features and development of coot. Acta Crystallogr. D Biol. Crystallogr. *66*, 486–501. https://doi.org/10.1107/S0907444910007493.

101. Liebschner, D., Afonine, P.V., Baker, M.L., Bunkóczi, G., Chen, V.B., Croll, T.I., Hintze, B., Hung, L.W., Jain, S., McCoy, A.J., et al. (2019). Macromolecular structure determination using X-rays, neutrons and electrons: recent developments in Phenix. Acta Crystallogr. D Struct. Biol. *75*, 861–877. https://doi.org/10.1107/S2059798319011471.

102. Chen, V.B., Arendall, W.B., 3rd, Headd, J.J., Keedy, D.A., Immormino, R.M., Kapral, G.J., Murray, L.W., Richardson, J.S., and Richardson, D.C. (2010). MolProbity: all-atom structure validation for macromolecular crystallography. Acta Crystallogr. D Biol. Crystallogr. *66*, 12–21. https://doi.org/10.1107/S0907444909042073.

103. Otwinowski, Z., and Minor, W. (1997). Processing of X-ray diffraction data collected in oscillation mode. Methods Enzymol. *276*, 307–326. https://doi.org/10.1016/S0076-6879(97)76066-X.

104. Terwilliger, T.C., Grosse-Kunstleve, R.W., Afonine, P.V., Moriarty, N.W., Zwart, P.H., Hung, L.W., Read, R.J., and Adams, P.D. (2008). Iterative model building, structure refinement and density modification with the PHENIX AutoBuild wizard. Acta Crystallogr. D Biol. Crystallogr. *64*, 61–69. https://doi.org/10.1107/S090744490705024X.

105. Afonine, P.V., Grosse-Kunstleve, R.W., Echols, N., Headd, J.J., Moriarty, N.W., Mustyakimov, M., Terwilliger, T.C., Urzhumtsev, A., Zwart, P.H., and Adams, P.D. (2012). Towards automated crystallographic structure refinement with phenix.refine. Acta Crystallogr. D Biol. Crystallogr. *68*, 352–367. https://doi.org/10.1107/S0907444912001308.

106. Guo, Y., Li, D., Zhang, S., Yang, Y., Liu, J.J., Wang, X., Liu, C., Milkie, D.E., Moore, R.P., Tulu, U.S., et al. (2018). Visualizing intracellular organelle and cytoskeletal interactions at nanoscale resolution on millisecond timescales. Cell *175*, 1430–1442.e17. https://doi.org/10.1016/j.cell.2018.09.057.

Please cite this article in press as: Qiu et al., Short-distance vesicle transport via phase separation, Cell (2024), https://doi.org/10.1016/j.cell.2024.03.003

STAR★METHODS

KEY RESOURCES TABLE

REAGENT or RESOURCE	SOURCE	IDENTIFIER
Bacterial and virus strains		
DH5α competent cells	Thermo Fisher	Cat#18263012
BL21-CodonPlus(DE3)-RIL cells	Agilent	Cat#230245
DH10Bac cells	Thermo Fisher	Cat#10361012
Chemicals, peptides, and recombinant proteins		
Alexa Fluor 647 NHS Ester	Thermo Fisher	Cat#A20106
iFluor 488 NHS Ester	AAT Bioquest	Cat#1023
Cy3 NHS Ester	AAT Bioquest	Cat#271
Cy5 NHS Ester	AAT Bioquest	Cat#280
DiO	AAT Bioquest	Cat#22066
DiI	AAT Bioquest	Cat#22102
DiIC18(5)-DS	AAT Bioquest	Cat#22054
16:0-18:1 PC (POPC)	Avanti Polar Lipids	Cat#850457P
18:1 PS (DOPS)	Avanti Polar Lipids	Cat#840035P
18:1 PI(4,5)P2	Avanti Polar Lipids	Cat#850155P
FuGENE® HD Transfection Reagent	Promega	Cat#E2311
Sf-900 III SFM medium	Thermo Fisher	Cat#12658027
Cocktail protease inhibitor	Bimake	Cat#B14002
PMSF	Sigma	Cat#P7626
Pepstatin A	Sigma	Cat#P5318
Sodium cholate	Sigma	Cat#27029
Sucrose	Merck	Cat#107651
HEPES	Roth	Cat#6763.3
Glycine	Merck	Cat#104201
Trypsin	Sigma	Cat#T9201
Aprotinin	Sigma	Cat#A1153
Paraformaldehyde	Sigma	Cat# 158127
Glutaraldehyde	Sigma	Cat# G5882
Osmium tetroxide	SPI	Cat#1250423
Uranyl acetate	EMS	Cat#22400
Lead citrate	Sigma	Cat#15326
EPON 812 resin	Sigma	Cat#45345
Latrunculin A	MedChemExpress	Cat#HY-16929
Nocodazole	MedChemExpress	Cat#HY-13520
RIM1α-N-LPETGG (aa 1-474-LPETGG)	Wu et al.[26]	N/A
GGG-RIM1α-C (aa 481-1334)	Wu et al.[26]	N/A
RIM1α-FL (aa 1-1334)	Wu et al.[26]	N/A
Sortase A-ΔN59 (aa 60-206)	Wu et al.[26]	N/A
RIMBP-(SH3)3 (aa 178-252 + 844-1040)	Wu et al.[26]	N/A
RIMBP-1st SH3 (aa 178-252)	Wu et al.[26]	N/A
RIMBP-2nd SH3 (aa 844-965)	Wu et al.[26]	N/A
RIMBP-3rd SH3 (aa 966-1040)	Wu et al.[26]	N/A
ELKS1 (aa 141-660 + 938-948)	Wu et al.[29]	N/A
ELKS1 (aa 419-623)	This paper	N/A

(*Continued on next page*)

Continued

REAGENT or RESOURCE	SOURCE	IDENTIFIER
ELKS1 (aa 436-623)	This paper	N/A
ELKS1 (aa 469-623)	This paper	N/A
ELKS1 (aa 510-623)	This paper	N/A
ELKS1 (aa 469-610)	This paper	N/A
ELKS1 (aa 469-610 D533R)	This paper	N/A
ELKS1 (aa 469-610 R543D)	This paper	N/A
ELKS1 (aa 469-610 K544D)	This paper	N/A
ELKS1 (aa 469-610 K551D)	This paper	N/A
ELKS1 (aa 469-610 R572D)	This paper	N/A
ELKS2 (aa 415-619)	This paper	N/A
Pclo (aa 3633-3769 + 4401-5068)	This paper	N/A
Pclo-2KE (aa 3633-3769 + 4401-5068 K4992/4994E)	This paper	N/A
Pclo-2DA (aa 3633-3769 + 4401-5068 D4651/4657A)	This paper	N/A
Pclo-PAB (aa 4401-5068)	This paper	N/A
Pclo-PRM (aa 3633-3668)	This paper	N/A
Pclo-C2A (aa 4618-4760)	This paper	N/A
Pclo-C2B (aa 4861-5068)	This paper	N/A
PAB-ΔC2A (aa 4401-4617 + 4761-5068)	This paper	N/A
PAB-ΔC2B (aa 4401-4932)	This paper	N/A
PAB-2KE (aa 4401-5068 K4992/4994E)	This paper	N/A
PAB-2DA (aa 4401-5068 D4651/4657A)	This paper	N/A
Pclo (aa 3623-3769)	This paper	N/A
Pclo (aa 3644-3769)	This paper	N/A
Pclo (aa 3668-3769)	This paper	N/A
Pclo (aa 3683-3769)	This paper	N/A
Pclo (aa 3683-3769 D3695R)	This paper	N/A
Pclo (aa 3683-3769 E3719R)	This paper	N/A
Pclo (aa 3683-3769 R3736D)	This paper	N/A
Pclo (aa 3683-3769 L3698R)	This paper	N/A
Pclo (aa 3683-3769 L3726R)	This paper	N/A
Pclo (aa 3683-3769 L3729E)	This paper	N/A
TFG (aa 1-400)	This paper	N/A
mEGFP-synapsin-FL (aa 1-706)	Wu et al.[29]	N/A
ITSN (aa 740-1214)	Wu et al.[29]	N/A
HRV-3C protease	Wu et al.[26]	N/A
TEV protease	Wu et al.[26]	N/A
Deposited data		
Pclo/ELKS complex structure	This paper	PDB: 8I3E
Mendeley Data	This paper	https://doi.org/10.17632/b69mjhr5yx.1
Experimental models: Cell lines		
Gibco® Sf9 cells	Thermo Fisher	Cat#12659017
COS7 cells	ATCC	Cat#CCL-70
HeLa cells	ATCC	Cat#CCL-2
293FT cells	Thermo Fisher	Cat#R70007
Recombinant DNA		
pET-32a	Novagen	Cat#69015-3

(*Continued on next page*)

Please cite this article in press as: Qiu et al., Short-distance vesicle transport via phase separation, Cell (2024), https://doi.org/10.1016/j.cell.2024.03.003

Continued

REAGENT or RESOURCE	SOURCE	IDENTIFIER
pFastBac	Thermo Fisher	Cat#10712024
pET28a-Sortase A-ΔN59 (aa 60-206)	Wu et al.[26]	N/A
HRV-3C protease	Wu et al.[26]	N/A
TEV protease	Wu et al.[26]	N/A
32m3c-RIM1α-N-LPETGG (aa 1-474-LPETGG)	Wu et al.[26]	N/A
32mTEV-GGG-RIM1α-C (aa 481-1334)	Wu et al.[26]	N/A
m3c-RIMBP-(SH3)3 (aa 178-252 + 844-1040)	Wu et al.[26]	N/A
32m3c-RIMBP-1st SH3 (aa 178-252)	Wu et al.[26]	N/A
32m3c-RIMBP-2nd SH3 (aa 844-965)	Wu et al.[26]	N/A
32m3c-RIMBP-3rd SH3 (aa 966-1040)	Wu et al.[26]	N/A
32m3c-ELKS1 (aa 141-660 + 938-948)	Wu et al.[29]	N/A
32m3c-ELKS1 (aa 419-623)	This paper	N/A
32m3c-ELKS1 (aa 436-623)	This paper	N/A
32m3c-ELKS1 (aa 469-623)	This paper	N/A
32m3c-ELKS1 (aa 510-623)	This paper	N/A
32m3c-ELKS1 (aa 469-610)	This paper	N/A
32m3c-ELKS1 (aa 469-610 D533R)	This paper	N/A
32m3c-ELKS1 (aa 469-610 R543D)	This paper	N/A
32m3c-ELKS1 (aa 469-610 K544D)	This paper	N/A
32m3c-ELKS1 (aa 469-610 K551D)	This paper	N/A
32m3c-ELKS1 (aa 469-610 R572D)	This paper	N/A
32m3c-ELKS2 (aa 415-619)	This paper	N/A
32m3c-Pclo (aa 3633-3769 + 4401-5068)	This paper	N/A
32m3c-Pclo-2KE (aa 3633-3769 + 4401-5068 K4992/4994E)	This paper	N/A
32m3c-Pclo-2DA (aa 3633-3769 + 4401-5068 D4651/4657A)	This paper	N/A
32m3c-Pclo-PAB (aa 4401-5068)	This paper	N/A
32m3c-Pclo-PRM (aa 3633-3668)	This paper	N/A
m3c-Pclo-C2A (aa 4618-4760)	This paper	N/A
m3c-Pclo-C2B (aa 4861-5068)	This paper	N/A
32m3c-PAB-ΔC2A (aa 4401-4617 + 4761-5068)	This paper	N/A
32m3c-PAB-ΔC2B (aa 4401-4932)	This paper	N/A
32m3c-PAB-2KE (aa 4401-5068 K4992/4994E)	This paper	N/A
32m3c-PAB-2DA (aa 4401-5068 D4651/4657A)	This paper	N/A
32m3c-Pclo (aa 3623-3769)	This paper	N/A
32m3c-Pclo (aa 3644-3769)	This paper	N/A
32m3c-Pclo (aa 3668-3769)	This paper	N/A
32m3c-Pclo (aa 3683-3769)	This paper	N/A
32m3c-Pclo (aa 3683-3769 D3695R)	This paper	N/A
32m3c-Pclo (aa 3683-3769 E3719R)	This paper	N/A
32m3c-Pclo (aa 3683-3769 R3736D)	This paper	N/A
32m3c-Pclo (aa 3683-3769 L3698R)	This paper	N/A
32m3c-Pclo (aa 3683-3769 L3726R)	This paper	N/A
32m3c-Pclo (aa 3683-3769 L3729E)	This paper	N/A
32m3c-TFG (aa 1-400)	This paper	N/A
pFastBac3c-mEGFP-synapsin-FL (aa 1-706)	Wu et al.[29]	N/A
32m3c-ITSN (aa 740-1214)	Wu et al.[29]	N/A

(*Continued on next page*)

Continued

REAGENT or RESOURCE	SOURCE	IDENTIFIER
Software and algorithms		
Image J	NIH	https://imagej.nih.gov/ij/
Prism	GraphPad	https://www.graphpad.com/scientific-software/prism/
Origin 7.0	OriginLab	https://www.originlab.com/
ASTRA 6	Wyatt	https://www.wyatt.com/products/software/astra.html
ARCIMBOLDO	Rodriguez et al.[99]	http://chango.ibmb.csic.es/lite
Coot	Emsley et al.[100]	https://www2.mrc-lmb.cam.ac.uk/personal/pemsley/coot/
PHENIX	Liebschner et al.[101]	https://phenix-online.org/
MolProbity	Chen et al.[102]	http://molprobity.biochem.duke.edu/
PyMOL	Schrodinger	https://www.pymol.org/
Other		
Superdex 75 26/60	GE Healthcare	Cat#28-9893-34
Superdex 200 26/60	GE Healthcare	Cat#28-9893-36
Superose 6 10/300 GL	Cytiva	Cat# 17517201
Superose 12 10/300 GL	Cytiva	Cat# 29036225
HiTrap desalting column	GE Healthcare	Cat#29-0486-84
NanoDrop™ One/One^{C} Microvolume UV-Vis Spectrophotometer	Thermo Fisher	Cat#ND-ONE-W
Controlled-pore glass bead (CPG-3000, glycerol coated)	LGC Biosearch GmbH	Cat#BG6-5002

RESOURCE AVAILABILITY

Lead contact

Further information and requests for resources and reagents should be directed to and will be fulfilled by the lead contact, Mingjie Zhang (zhangmj@sustech.edu.cn)

Materials availability

This study did not generate new unique reagents.

Data and code availability

- The atomic structure of Pclo-CC3/ELKS1-CC complex has been deposited to and released by the Protein Data Bank under the accession code PDB: 8I3E.
- Raw data from Figures 1, 2, 3, 5, 6, 7, S1–S3, and S5–S7 were deposited on Mendeley at https://doi.org/10.17632/b69mjhr5yx.1.
- Any additional information required to reanalyze the data reported in this work paper is available from the lead contact upon request.
- Data and software availability information is detailed in the "key resources table" of the manuscript.

EXPERIMENTAL MODEL AND STUDY PARTICIPANT DETAILS

Bacterial strain

Escherichia coli BL21-CodonPlus(DE3)-RIL cells (Agilent) were used in this study to express all the recombinant proteins except for synapsin. Transfected cells were cultured in LB medium supplemented with necessary antibiotics at 37°C with 220 rpm shaking and expressed at 16°C with 220 rpm shaking.

DH10Bac cells (ThermoFisher) were used to generate recombinant bacmid. Cells were cultured in LB medium supplemented with necessary antibiotics at 37°C with 220 rpm shaking.

Please cite this article in press as: Qiu et al., Short-distance vesicle transport via phase separation, Cell (2024), https://doi.org/10.1016/j.cell.2024.03.003

Cell line

Gibco® Sf9 cells (ThermoFisher) were used in this study to generate baculovirus and express synapsin. Cells were cultured in Sf-900 III SFM medium (ThermoFisher) at 27°C. For virus preparation, adherent culture was used. For protein expression, suspension culture with 100 rpm shaking was applied.

METHOD DETAILS

Genes and plasmids

The mouse Piccolo cDNA (Genbank: NM_011995.4) constructs were assembled using partial cDNA clones provided by Dr. Johann Helmut Brandstätter at Friedrich-Alexander-Universität Erlangen-Nürnberg, Germany. Rat RIM1α (Genbank: XM_017596673.1) and rat RIMBP2 (Genbank: XM_017598284.1) genes were kindly donated by Dr. Pascal S. Kaeser from Harvard Medical School. Rat ELKS1 (Genbank: NM_170788.2), mouse ELKS2 (Genebank: XR_001781113.2), and mouse synapsin 1α (Genbank: NM_013680.4) were cloned from rat and mouse brain libraries. Human Intersectin 1 was purchased from Addgene (Addgene #47395, GenBank: AF114487.1). Human TFG (Genbank: NM_006070.6) was synthesized.

Constructs of RIM, RIMBP, ELKS, synapsin, and ITSN were generated in our previous study.[29] Briefly, all these genes, Pclo fragments and mutants, and TFG (except for synapsin) were amplified by standard PCR and cloned into a modified pET-32a vector containing an N-terminal Trx-6xHis tag and an HRV-3C protease digestion site. Synapsin was expressed with insect cells. Full length synapsin gene was inserted into a modified pFastBac vector with an N terminal EGFP-6xHis tag and an HRV-3C protease digestion site. All constructs were verified by DNA sequencing.

Protein expression and purification

RIM, RIMBP, ELKS, synapsin, and ITSN proteins expression and purification were described in our earlier study.[29] Briefly, RIMBP, ELKS, ITSN, Pclo, and TFG were directly expressed with *Escherichia coli* BL21-CodonPlus(DE3)-RIL cells (Agilent). Transfected cells were cultured in LB medium at 37°C with 220 rpm shaking until OD_{600} reached ~ 0.8, protein expression was induced by 0.25 mM IPTG after cooling down to 16°C. The induced cells were grown at 16°C with 220 rpm shaking overnight. Cell pellets were harvested by centrifuge and lysed by high pressure homogenization in binding buffer containing 50 mM Tris pH 8.0, 1000 mM NaCl, 5 mM Imidazole, and supplemented with 1 mM PMSF. The homogenates were purified using Ni^{2+}-NTA Sepharose (GE Healthcare) affinity column and eluted with 50 mM Tris pH 8.0, 500 mM NaCl, 300 mM imidazole. The eluted proteins were immediately further purified by size exclusion chromatography using HiLoad 26/600 Superdex 200pg column, pre-equilibrated in a buffer containing 50 mM Tris pH 8.0, 300 mM NaCl, 1mM EDTA,1mM DTT. Affinity tag was cleaved by HRV-3C protease at 4°C overnight and removed by another step of size exclusion chromatography. The column was pre-equilibrated with HEPES buffered saline (x HBS: 20 mM HEPES pH 7.5, x mM NaCl, 1 mM TCEP) with different concentration of NaCl according to their biochemical properties of individual proteins. 100 mM, 100 mM, 200 mM, and 300 mM NaCl were applied for RIMBP, ITSN, ELKS, and Pclo, respectively. Proteins were concentrated with Amicon ultra centrifugal filter (MWCO = 10 kD, Millipore) to ~ 10 mg/ml and aliquot to small fractions. Proteins were then flash frozen in liquid nitrogen and moved to -80°C for long term storage.

Full length RIM purification was described in our previous study.[26] Briefly, RIM N-terminal fragment (1-474) fused with an "LPETGG" tag at its C-terminal end, C-terminal fragment RIM (481-1334) with a "GGG" site at its N-terminal end, and the protein ligase – sortase ΔN59 were purified from E. coli similar to the description above. The N-terminal fragment, C-terminal fragment, and sortase were mixed at 2:1:1 molar ratio and supplemented with 10 mM $CaCl_2$ to initiate ligation. After 2h incubation at room temperature, full length RIM was purified by HiLoad 26/600 Superdex 200pg size exclusion chromatography with 300 HBS.

Synapsin was expressed in Sf9 cells as described in our previous study.[29] pFastBac-mEGFP-Syn plasmid was transformed into DH10Bac cells to produce recombinant Bacmid. The Bacmids were then transfected into Sf9 cells using FuGENE® HD Transfection Reagent (Promega) to produce the first generation of recombinant baculovirus (P1). P1 virus was used to generate P2 and P3 virus sequentially. To estimate the viral titer and optimal virus concentration for expression, we infected small scale Sf9 cells with gradient amount of P3 virus and used western blot to monitor protein expression level. For large scale culture, 600 ml Sf9 cells were cultured in 2 L flask at 27°C with 100 rpm shaking. A suitable amount of P3 virus was added to the culture when cell density reached ~ 1.5 * 10^6/ml. Cells were cultured for another 60 h under the same culture condition. Cells were harvested by centrifugation at moderate speed (1000 g * 10 min) and resuspended in the binding buffer supplemented with 1x cocktail protease inhibitor (Bimake). Then high-pressure homogenization was applied, and the homogenates were purified by Ni^{2+}-NTA Sepharose (GE Healthcare) affinity column followed by HiLoad 26/600 Superdex 200pg size exclusion chromatography pre-equilibrated in 100 HBS similar to proteins purified from E. coli.

Fluorophore labelling of proteins

Fluorescent labeling dye iFluor 488/Cy3/Cy5 NHS easters (AAT Bioquest) were dissolved in DMSO at 10 mg/ml concentration. Proteins were concentrated to 5 ~ 10 mg/ml mass concentration in HBS at pH 7.5 to ensure specific N-terminal labelling by each fluorophore, and the dye to protein molar ratio was adjusted to 1 : 1 for each reaction. Normally, ~ 1 μl dye was required for labelling 100 μl protein at the 100 μM concentration. Additional NaCl does not affect labelling reaction and thus can be used to improve protein stability when necessary. With gentle shaking at room temperature for 1 h in dark, the reaction was quenched by adding 200 mM Tris.

Please cite this article in press as: Qiu et al., Short-distance vesicle transport via phase separation, Cell (2024), https://doi.org/10.1016/j.cell.2024.03.003

Labeled proteins were centrifugated to remove any precipitation and exchanged to HBS using a HiTrap desalting column (GE Healthcare). Fluorescence labeling efficiency was determined by NanoDrop One^{C} (Thermo scientific). For imaging assay, sparse labelling was used. Normally we used 2% labelling ratio except for Pclo, which was at 5% to reduce laser power during imaging, as we observed that strong laser illumination reduced mobility of Pclo-containing condensates.

Small Unilamellar Vesicle (SUV) preparation

Majority SUVs used in this study composed of 77% POPC, 20% DOPS, 1% PIP2, and 2% fluorescent dye (DiO or DiI) unless otherwise specified. The neutralized SUVs were composed of 98% POPC and 2% DiO. All lipid powders were purchased from Avanti Polar Lipids. Lipids were dissolved in chloroform and mixed in desired molar ratio in a glass vial. The lipid mixture was then dried under nitrogen stream and subject to vacuum for at least 1 h to remove all residual chloroform. Dried lipid films were hydrated in 100 HBS supplemented with 1% sodium cholate (Sigma). Brief pipetting and vortexing could dissolve the lipid films thoroughly and the solution turned transparent. The lipid solution was later loaded to a HiTrap desalting column (GE Healthcare) equilibrated with 100 HBS. SUVs were spontaneously formed during the detergent removal process. The SUV concentration (refer to the lipid concentration) was estimated by measuring the dye concentration using NanoDrop One^{C} (Thermo scientific).

Phase separation assays: sample preparation and imaging

All proteins used for imaging were centrifuged at 16,900 g for 10 min at 4°C to remove potential aggregation or precipitation before performing experiments. The concentration of proteins and vesicles, and buffer conditions were marked at the corresponding figures and legends. Samples were injected into a home-made chamber made up of a coverslip and a glass slide assembled by two parallel double-sided tapes with 0.15 mm thickness. The chamber was sealed immediately by vacuum grease (Dow Corning) after sample loading except when further manipulation was required (e.g., addition of Ca2+ or EDTA). Differential interference contrast (DIC) images (Figures 2A, 2B, S2A, and S2E) were captured by a Nikon Ni-U upright fluorescence microscope with a 60x oil lens. All other images were captured by a Zeiss LSM 880 confocal microscope with a 63x oil lens.

For Pclo/SUV phase separation assays (Figure 2), Pclo and SUVs were mixed at desired concentration with or without 1 mM Ca2+ in a microcentrifuge tube. After 5 min incubation, samples were injected into the chamber and settled down for ~ 15 min to reach equilibrium before images were taken. For droplets coalescing experiment (Figure 2B), continuous images were captured once majority droplets were settled down to the glass bottom. For vesicle extraction experiments (Figure 1), synapsin, Pclo, vesicles (SUVs or SVs), and ITSN were sequentially mixed (before ITSN injection, there was no phase separation occurred). For Ca^{2+} treatment group, 1 mM Ca^{2+} was applied after protein and vesicle mixing. For monitoring the dynamic processes vesicle extraction by Pclo (Figure 1D), protein and SUV mixture was loaded into a chamber without sealing the chamber at first, Ca^{2+} or EDTA was directly injected into the system from one edge of the chamber after 15 min equilibration of the mixtures. Then time-lapse images were captured with a 15 s space to monitor the dynamic processes. For vesicle tethering assays (Figure 5), RIMBP, ELKS, Pclo, RIM, and vesicles, with or without Ca^{2+}, were sequentially mixed in a microcentrifuge tube. The mixture was loaded into a chamber and equilibrated for 5 ~ 10 min before images were taken. For Figure 5E, active zone condensates composed of RIM, RIMBP, and ELKS were loaded into a chamber first, Pclo/SUV condensates were prepared in another microcentrifuge tube simultaneously. After 5 min incubation, Pclo/SUV condensates were injected into the active zone condensates from one edge of the chamber. Images were continuously taken with a 15 s space to monitor the dynamic redistribution of components. For the final reconstitution assays (Figure 6), RIMBP, ELKS, Pclo, RIM, and synapsin, vesicles, ITSN, with or without Ca^{2+} were sequentially mixed in a microcentrifuge tube. After 5 min incubation in the tube, the samples were loaded into a chamber and waited for another 15 min before images were taken. For monitoring the vesicle transport process (Figure S5C), reconstituted condensates were loaded into a chamber first, then Ca^{2+} was injected from one edge of the chamber after 15 min equilibration. Time-lapse images with a 15 s interval between each image were immediately captured.

Fluorescence recovery after photobleaching (FRAP) assay

For each FRAP experiment, three regions of interest (ROIs) with exactly the same size were selected. ROI1 marked the site where photobleaching was applied, ROI2 marked another comparable droplet for correction of system fluorescent intensity fluctuations during imaging, and ROI3 was selected in the surrounding dilute solution for background correction. A circle with a 10-pixel (pixel size = 0.13 μm) diameter at the center of a droplet with about a 45-pixel diameter was selected. Three images were taken before photobleaching. Laser beams at 561 nm or 633 nm wavelengths were applied for Cy3 or Cy5 fluorophore, respectively, to bleach ROI1 till the fluorescent intensity reached the level comparable to that of ROI3. Time lapse images with 15 s intervals were taken for 10 min to record fluorescence intensity recovery. If second photobleaching was required to evaluate the mobile fraction in a droplet, same photobleaching protocol was applied to ROI1. Images were analyzed by ImageJ, the fluorescence intensity before photobleaching was set as 1. Data were expressed as mean ± SD.

Liposome binding assay

Brain total lipid extract (Avanti Polar Lipids) was dissolved in chloroform to 10 mg/ml and stored at -20°C. For each experiment, 2.5 mg total lipid extract was dried under nitrogen stream followed by 1 h vacuuming to remove residual chloroform. The dried lipids were hydrated in 1 ml Tris buffered saline (TBS, 50 mM Tris pH 8.0, 100 mM NaCl, 1 mM EDTA, and 1 mM DTT) with extensive

Please cite this article in press as: Qiu et al., Short-distance vesicle transport via phase separation, Cell (2024), https://doi.org/10.1016/j.cell.2024.03.003

pipetting and vortexing for ~ 10 min. Then liposomes were prepared via sonication (Branson 250 Sonifier, duty circle: 50%, output control: 5). The emulsion gradually became semi-transparent, indicating liposome formation. The solution was centrifuged at 5000 g for 15 min to remove large aggregates. The liposome concentration was estimated by the initial input, assuming there was no weight loss during the preparation.

For liposome binding, 5 μM Pclo (or its mutants) was mixed with 2 mg/ml liposome in TBS at 40 μl volume, after 30 min incubation at room temperature, 40 μl mixture was ultracentrifuged at 55,000 rpm (136,600 g) for 30 min to precipitate all liposomes. The supernatant was collected as sample S, and the pellet was washed twice with TBS before resuspended in 40 μl same buffer. Supernatant and pellet samples were analyzed by SDS-PAGE with Coomassie blue staining. Each experiment was repeated three times. The band intensity on SDS-PAGE gel was quantified by ImageJ and data were presented as mean ± SD.

Synaptic vesicle (SV) purification, labeling, and trypsin digestion

SV purification was described in our previous study.[29] In brief, 20 rat brains were homogenized in pre-cooled lysis buffer containing 320 mM sucrose, 4 mM HEPES pH 7.4, 0.2 mM PMSF, 1 mg/ml pepstatin A. 10 min brief centrifugation at 900 g removed cell debris. Then the supernatant was further centrifuged at 12,000 g for another 10 min. Pellet fraction containing the synaptosome was collected and washed with sucrose buffer (320 mM sucrose, 4 mM HEPES pH 7.4). Synaptosomes were then subject to 9 volumes of distilled water for hypoosmotic shock, and immediately buffered by 5 mM HEPES pH 7.4, 0.2 mM PMSF, and 1 mg/ml pepstatin A. SVs were liberated from the lysed synaptosomes and were collected from the supernatant after 20 min centrifugation at 14,500 g. Another step of ultrafast centrifugation at 230,000 g for 2 h resulted in accumulation of SVs in the pellet. The SV containing pellet fraction was resuspended in 40 mM sucrose and subject to a 50 ~ 800 mM sucrose gradient centrifugation at 110,800 g for another 3 h. The collected SV fraction were then run through a self-packed size exclusion chromatography (300 nm diameter glass beads) equilibrated with 300 mM glycine, 5 mM HEPES pH 7.4. SV fractions were pooled together and concentrated by centrifugation at 230,000 g for 2 h. The pellet was resuspended with 400 μl sucrose buffer. The estimated concentration was 2.5 mg/ml. The SVs were aliquoted into 20 fractions and stored at -80°C after flash freeze in liquid nitrogen.

For SV labeling, amphiphilic dye DiIC18(5)-DS (AAT Bioquest) was directly dissolved in aqueous SV buffer containing 20 mM HEPES pH7.5, 100 mM KCl, 1mM TCEP with rigorous vortexing. The mixture was centrifuged at 16,900 g for 10 min, and the supernatant containing the saturated concentration of DiIC18(5)-DS was collected for SV labeling. An aliquot of SV (2.5 mg/ml, 20μl) was thawed on ice followed by 16,900 g centrifugation for 10 min at 4°C to remove aggregates. Equal volume of DiIC18(5)-DS (20 μl) was mixed with SV supernatant by gentle pipetting and then moved to 37°C water bath incubation for 30 min. The mixture was centrifuged at 16900 g at 4°C for 30 min to remove precipitates. The supernatant was collected and added with another 60 μl SV buffer to a final volume of 100 μl corresponding to 0.5 mg/ml SV stock for immediate use. The labeled SVs were used within one day.

When trypsin digestion was needed, labeled SVs were mixed with 0.25% v/v 10 mg/ml (~ 400 μM) trypsin (Sigma) stock in 50 mM acetic acid. The digestion reaction was performed at room temperature for 3 h and quenched by adding 0.25% v/v 10 mg/ml (1.5 mM) aprotinin (Sigma) stock prepared in 50 mM MES pH 6.5, 150 mM NaCl for another 1 h incubation at room temperature.

Isothermal titration calorimetry (ITC) assay

ITC experiments were carried out on a MicroCal VP-ITC calorimeter (Malvern). All proteins were prepared in the same reaction buffer containing 20 mM Tris pH 8.0, 150 mM NaCl, 1 mM EDTA, and 1 mM DTT. The protein loaded in syringe was highly concentrated (normally 200 ~ 500 μM) for titrating into its binder in the reaction cell typically at 20-50 μM. Protein concentrations used were denoted in corresponding figure legends. Reaction was performed at 25°C. Each titration point injected 10 μl syringe protein into the cell within 20 s, followed by 120 s equilibrium. A titration curve contained a total of 27 titration points. Each titration curve was fitted with the one-site binding model using Origin 7.0 to obtain dissociation constant (K_d) and binding stoichiometry N.

Size exclusion chromatography coupled with multiangle light scattering (SEC-MALS) assay

The SEC-MALS assay was conducted by a platform composed of a multi-angle light scattering (MALS) detector (miniDawn, Wyatt), a differential refractive index (dRI) detector (Optilab, Wyatt) and a Liquid chromatography (LC) system (AKTA pure, GE Healthcare). For each assay, 200 μl sample (individual proteins or complexes) was injected via injection loop (100 μl) into a Superose 6 10/300 GL column or a Superose 12 10/300 GL column (GE Healthcare) pre-equilibrated with TBS. Data were analyzed by ASTRA6 (Wyatt).

Protein crystallization and structure determination

Crystals of the Pclo/ELKS1 complex were obtained by sitting drop vapor-diffusion method at 16 °C. The complex solution composed of 750μM Pclo 3683-3769 and 1000μM ELKS1 469-610 was mixed with equal volume (1 μL + 1 μL) of the reservoir buffer containing 0.1 M Sodium Formate pH 7.0, 12 % (w/v) PEG 3350 for crystallization.

Crystals were cryoprotected with 25 % (v/v) glycerol and flash-cooled to 100 K. X-ray diffraction data were collected at the BL19U1 beamline at the Shanghai Synchrotron Radiation Facility (SSRF). Diffraction data were processed using HKL2000.[103] The initial model was found using the ab initio phasing program ARCIMBOLDO.[99] Subsequent model auto-building was carried out by phenix.autobuild.[101,104] Further model building and refinement were carried out iteratively using Coot[100] and phenix.refine.[101,105] The final models were validated by MolProbity[102] and statistics were summarized in Table S1. All figures in the paper were prepared using PyMOL (https://www.pymol.org/).

Generation of stable cell lines expressing mCherry-TFG or EGFP-TFG

For generation of mCherry-TFG or EGFP-TFG expressing COS7 or HeLa stable cell lines, the pLenti-EF1a-mCherry-TFG or pLenti-EF1a-EGFP-TFG plasmid, together with three packaging plasmids (pLP1(gag/pol), pLP2 (rev) and pLP/VSV-G (VSV-G envelope), were co-transfected into 293FT cells. After 48 hours, the supernatant (containing the viral particles) was harvested and clarified by centrifuging at 3200g for 15 minutes at 4°C. Clarified lentivirus supernatant was then added into cell culture medium containing 8 μg/mL polybrene. Cells were further cultured for 48 hours. Single cell clones expressing mCherry-TFG or EGFP-TFG were then selected by fluorescence-activated cell sorting (FACS).

Multi-modal SIM (multi-SIM) live cell imaging

The multi-SIM system integrates TIRF-SIM, grazing incidence (GI-SIM)[106] and 3D-SIM, as well as lattice light sheet microscopy (LLSM). Nonlinear SIM achieves an optical resolution of 61.2 nm at a frame rate of more than 20 Hz. GI-SIM achieves an imaging speed of up to 684 Hz for 60,000 frames. This multi-modal SIM system allows us to select the optimum imaging mode for a specific process according to its subcellular location, dynamics, duration, etc. The NA of the multi-SIM lens is 1.49 (Nikon CFI SR HP Apo TIRF 1003/1.49 Oil objective lens).

For multi-SIM imaging experiments, COS7 stable cells transfected with the indicated plasmids were seeded onto Mattek glass-bottomed dishes 18-24 hours prior to imaging. Cells were maintained in 37°C and 5% CO2 during imaging. Multi-SIM images were analyzed by Image J.

Correlative light and electron microscopy

HeLa cells stably expressing mCherry-TFG were initially seeded onto a gridded glass-bottom dish (Cellvis, D35-14-1.5GI). After 24-hour culture, the cells were fixed with 4% paraformaldehyde at room temperature for 20 minutes. Fluorescence imaging was conducted using a Zeiss LSM980 Airyscan2 microscope. Bright-field microscopy was used to capture the cell morphology and ROI coordinates. Subsequently, the fixed cells underwent a secondary fixation step involving 2.5% glutaraldehyde treatment for 1 hour at room temperature, followed by a triple wash with 0.1 M phosphate buffer each lasting 15 minutes. Post-fixation staining was achieved by incubating the cells with 1% osmium tetroxide (SPI, 1250423) for 30 minutes on ice. Afterward, the cells were subjected to a triple wash with ultrapure water, followed by an overnight incubation in 1% aqueous uranyl acetate (EMS, 22400) at 4°C. Following another triple wash with ultrapure water, the cells were dehydrated using a graded ethanol series at low temperature (50%, 70%, 80%, 90%, 100%, 100%, 100%, 100%; 2 minutes each step). Subsequently, the cells were infiltrated with EPON 812 resin in the following ratios: 1:1 (v/v) resin and ethanol for 8 hours, 2:1 (v/v) resin and ethanol for 8 hours, and 3:1 (v/v) resin and ethanol for 8 hours. This was followed by two steps of pure resin infiltration for 8 hours each. Finally, the samples were placed in fresh resin and polymerized in an oven at 60°C for 48 hours. To facilitate the identification of ROIs on the resin surface, grids were engraved on the resin. The samples from the identified ROIs were sectioned into slices that were 80 nm inthickness and subsequently stained with uranyl acetate and lead citrate (C1813156). These stained sections were then examined using the HT-7800 120kV transmission electron microscope. Finally, the fluorescence images and TEM images were superimposed using Zeiss Zen Blue software.

QUANTIFICATION AND STATISTICAL ANALYSIS

For Pearson's correlation coefficient (PCC) quantification (Figures 1D, 1H, 2I, 6D, S1N, and S2I), we took 5 images and arbitrarily picked 10 droplets from each image (50 droplets in total) for analysis. Droplet boundary can be easily demarcated by synapsin. At least three batches of repeats were performed for each imaging experiment described in this manuscript. ImageJ with JACoP plugin was used to generate the PCC value. Then GraphPad Prism was used to do the quantification.

For PcloC/SUV phase separation capacity comparison (Figures 2A and 2D), we quantified the total droplet area and number of the pictures (1212 x 1212 pixels, pixel size = 0.122 μm) of each group using ImageJ. Each experimental group was repeated three batches, and three pictures of each batch were analyzed for quantification (9 pictures in total for each group). For liposome binding assay (Figure S3D), the SDS-PAGE gel was analyzed by ImageJ, the intensity of each band was measured and calculated. Three batches of experiments were repeated.

For measurement of SUV or SV coating efficiency on the reconstituted active zone condensates (Figures 5D, 5I, 6D, S5G, and S5L), a total of 5 images with 10 arbitrarily selected droplets from each image (50 droplets each group) were analyzed. An 8 μm arc was drawn along the SUV coating region, and the mean fluorescence intensity of the arc was plotted as one data point for each droplet. For the groups with enriched SUV patches, the arc was drawn on the SUV enriched region to derive the data point.

Statistical analysis was performed with GraphPad Prism 7.0. Data were expressed as mean ± SD. One-way ANOVA with Dunnett's multiple comparisons test was applied. ns (not significant), $p > 0.05$; ****, $p < 0.0001$. N value was reported in corresponding figure legends.

Supplemental figures

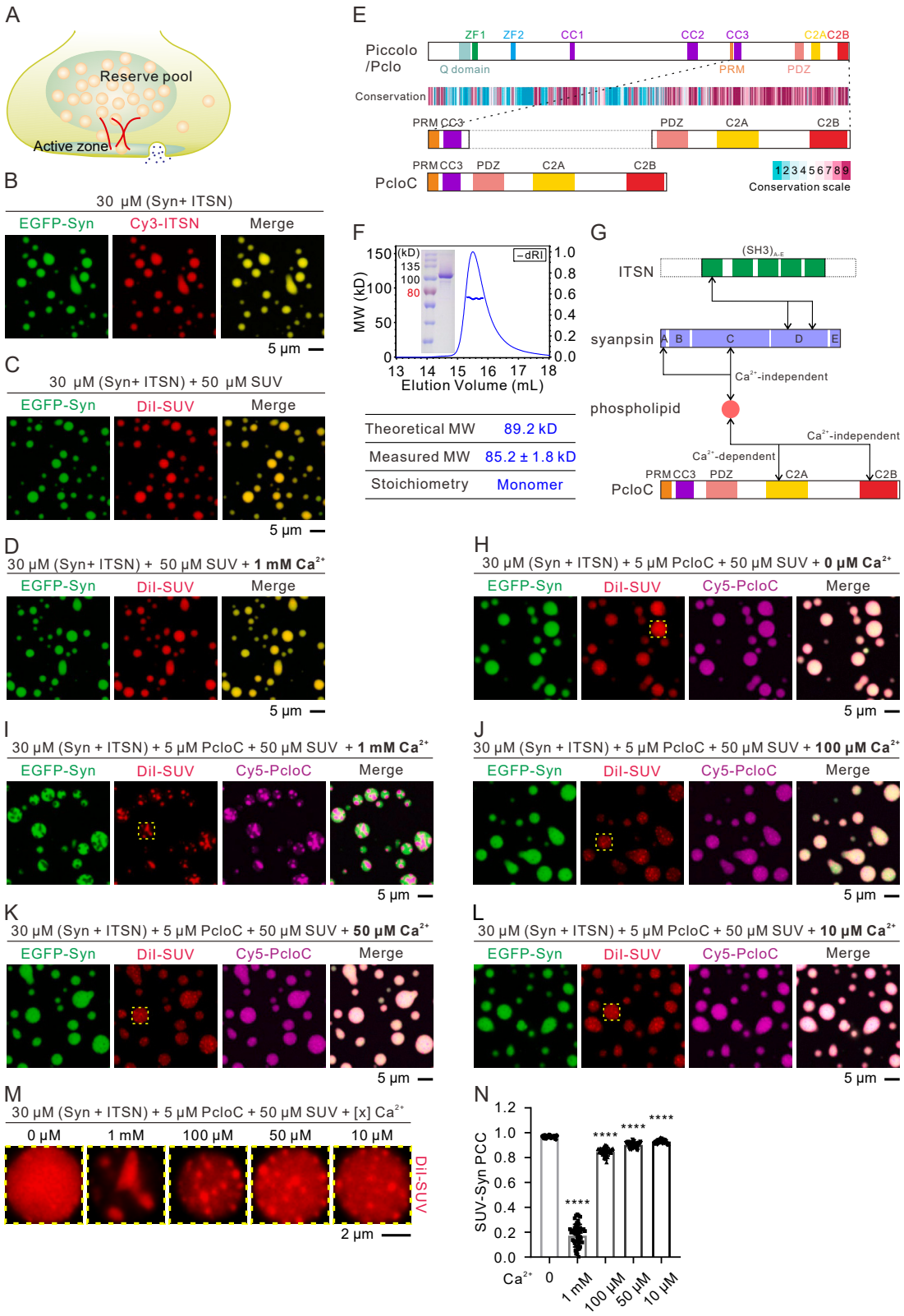

(legend on next page)

Figure S1. PcloC, but not synapsin, responds to Ca^{2+} and triggers SV redistribution, related to Figure 1

(A) A schematic diagram showing the reserve pool condensate and the active zone condensate in a presynaptic bouton. The majority of SVs are maintained in the reserve pool, and only a few SVs coat the surface of the active zone for activity-induced fusion with the plasma membrane. Red lines represent Pclo molecules that are known to position perpendicularly with respect to the plasma membrane and to connect the active zone and the reserve pool and thereby may contribute to SV shuttling from the reserve pool to the active zone.

(B) Confocal images showing the condensate formed by synapsin and ITSN in the imaging buffer with 100 mM NaCl without containing any crowding agent.

(C) Coacervation of SUVs with the synapsin/ITSN condensate described in (B).

(D) Same composition as (C), but with inclusion of 1 mM Ca^{2+} in the buffer. The synapsin/ITSN/SUV condensate did not respond to Ca^{2+} treatment.

(E) Schematic diagram showing the sequence features of Piccolo. The first line depicts the domain organization of the full-length Pclo; the second line shows the amino acids conservation of Pclo throughout the evolution; the third line shows the zoom-in domain organization of a highly conserved Piccolo-C-terminal fragment; and the last line shows the domain organization of the PcloC protein used in this study, which consists of a PRM motif, a CC3 domain, and a PDZ-C2A-C2B tandem.

(F) SEC-MALS (left) and SDS-PAGE (right) characterization of purified PcloC. PcloC is a stable monomer in solution. SDS-PAGE shows the quality of purified PcloC.

(G) Interaction network among synapsin, ITSN, phospholipid, and PcloC.

(H–L) Same setting as Figure 1A, except for performing the experiment with a Ca^{2+} concentration gradient of 0, 10, 50, 100, and 1,000 μM as indicated.

(M) Zoom-in of a highlighted region (dashed box) of the SUV channel as indicated in (H)–(L). The higher magnification clearly shows a heterogeneous distribution of SUVs after Ca^{2+} treatment.

(N) PCC quantification of the correlation between SUV and synapsin, in the absence or presence of different concentrations of Ca^{2+}.

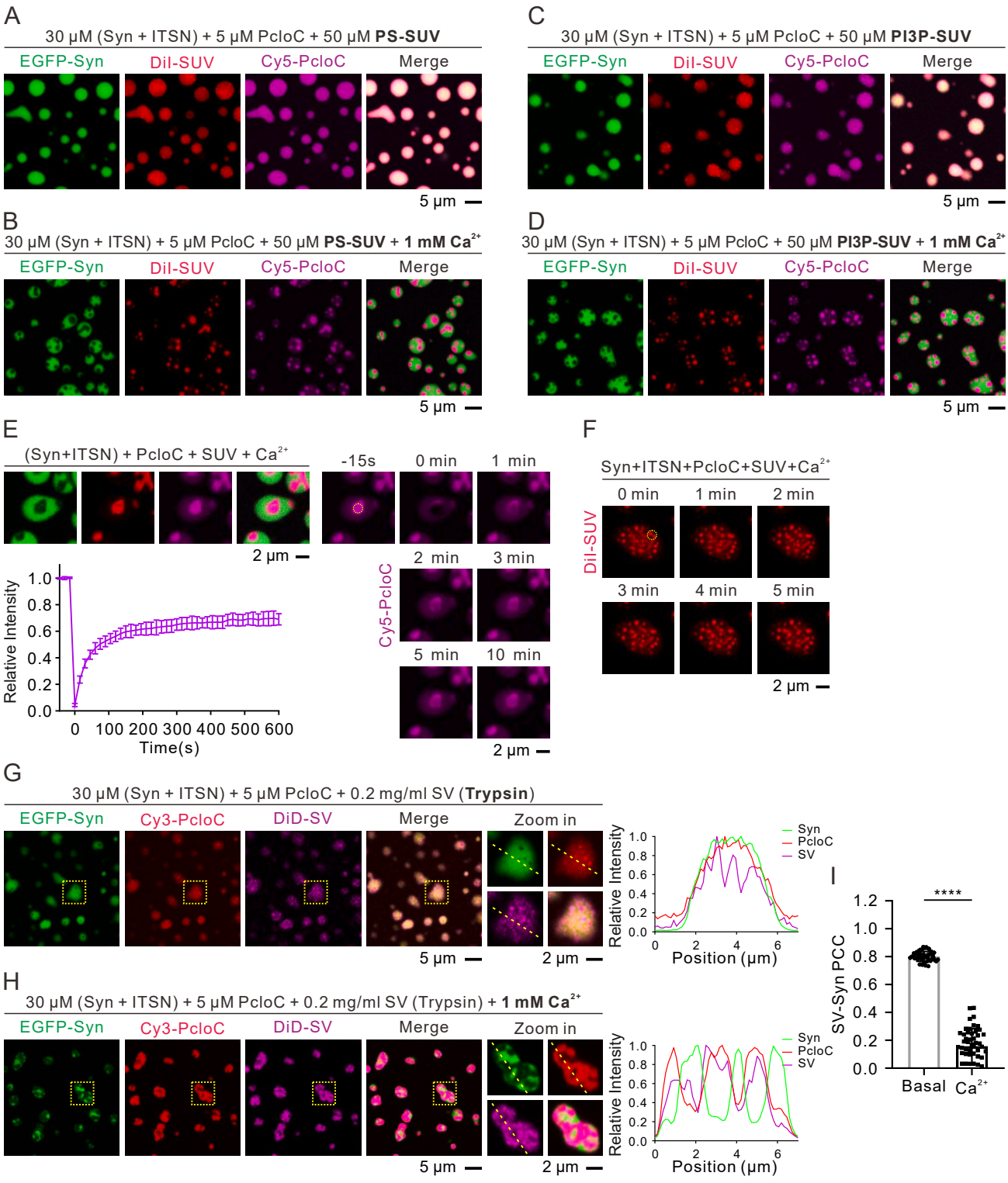

Figure S2. PcloC can extract negatively charged SUVs or SVs with the surface proteins removed by trypsin digestion from the synapsin phase, related to Figure 1

(A and B) PS-SUV (78% POPC + 20% DOPS + 2% DiI) homogeneously distributed in the synapsin/ITSN/PcloC condensate (A), and SUVs were extracted out from the synapsin condensate by PcloC upon Ca^{2+} treatment (B).

(legend continued on next page)

(C and D) PI3P-SUV (77% POPC + 20% DOPS + 1% PI3P + 2% DiI) homogeneously distributed in the synapsin/ITSN/PcloC condensate (C). SUVs were extracted out from the synapsin condensate by PcloC upon Ca^{2+} treatment (D).

(E) FRAP analysis of Cy5-labeled PcloC in the mixture of synapsin/ITSN/SUV/PcloC after 1 mM Ca^{2+} treatment. A yellow dashed circle with a 10-pixel (pixel size = 0.13 μm) diameter was selected for photobleaching (see the circle marked in the image acquired at −15 s). Droplet number n = 6 was used to construct the FRAP curve. Data are presented as mean ± SD.

(F) Time-lapse confocal images showing that small SUV clusters formed after Ca^{2+} injection can coalesce upon contacting each other (see two clusters highlighted with a yellow circle in the image marked as 0 min), indicating that SUVs remain dynamic after Ca^{2+}-mediated redistribution.

(G and H) Representative images of trypsin-digested SV distribution in the condensate formed by synapsin, ITSN, and PcloC, in the absence (G) or presence (H) of Ca^{2+}.

(I) Quantification of PCC between SV and synapsin for (G) and (H).

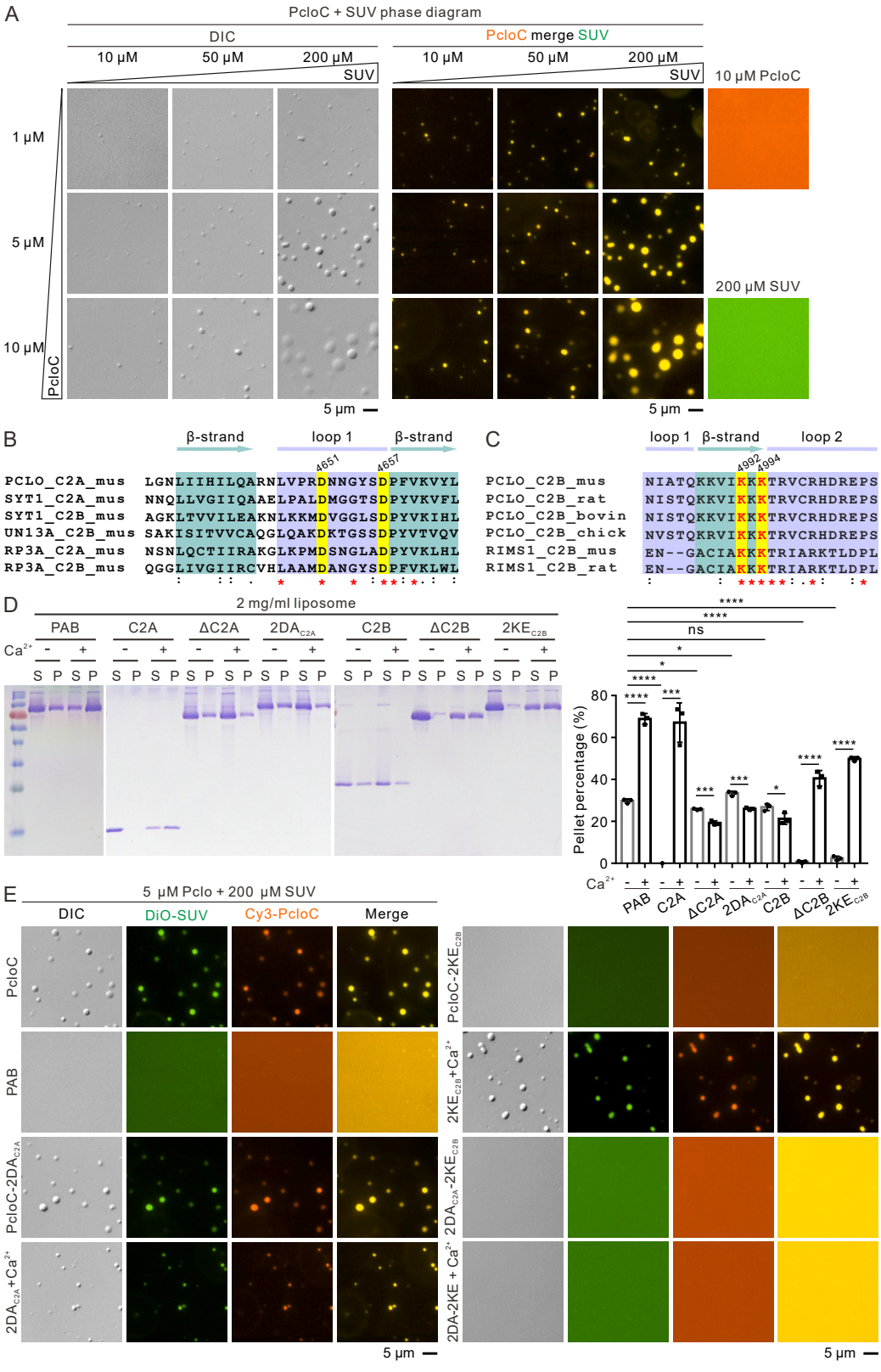

(legend on next page)

Figure S3. Both C2A and C2B of Pclo are involved in Pclo-mediated extraction of vesicles from the synapsin condensate, related to Figure 2

(A) DIC and merged fluorescence images showing the phase diagram of the PcloC and SUV mixtures as functions of the two-component concentrations. The molar concentration of SUV is calculated as the total lipid concentration. The average molecular weight of lipids is ~1,000 g/mol (1 kDa) or less. A concentration of 200 μM lipid mixture corresponds to ~0.2 mg/mL of lipids by mass.

(B) Amino acid sequence alignment of mouse Pclo-C2A domain with several other known Ca^{2+} binding C2 domains, including both C2A and C2B domains of mouse synaptotagmin 1 (UniProt: P46096), C2B domain of mouse Munc 13-1 (UniProt: Q4KUS2), and both C2A and C2B domains of mouse rabphilin 3A (UniProt: P47708). Two Asp residues (D4651 and D4657) in the loop 1 region of Pclo critical for Ca^{2+} binding are highlighted in yellow.

(C) Amino acid sequence alignment of mouse Pclo-C2B with several other C2 domains that are known to be deficient in Ca^{2+} binding: the C2B domain of rat (UniProt: Q9JKS6), bovine (UniProt: A0A3Q1M9D0), chick (UniProt: Q9PU36) Pclo, and the C2B domain of mouse (UniProt: Q99NE5), rat (UniProt: Q9JIR4) RIM1α. Two Lys residues (K4992, K4994) in the β strand critical for binding to negatively charged lipid membranes are highlighted in yellow.

(D) Representative SDS-PAGE images showing the results of PcloC and its variants in binding to liposomes. In each assay, 5 μM PAB, C2A, PAB-ΔC2A, PAB-$2DA_{C2A}$, C2B, PAB-ΔC2B, or PAB-$2KE_{C2B}$ were mixed with 2 mg/mL of liposome with or without 1 mM Ca^{2+} in the assay buffer. After high-speed centrifugation, the supernatant and pellet fractions were analyzed by SDS-PAGE with Coomassie blue staining. The pellet fractions representing the liposome-bound proteins were quantified and shown on the right. Data are presented as mean ± SD. One-way ANOVA with Dunnett's multiple comparisons test was used. ns, not significant, $p > 0.05$; *$p < 0.05$; ***$p < 0.001$; ****$p < 0.0001$.

(E) DIC and fluorescence images showing phase separation ability of different PcloC variants with SUVs. Schematic domain diagrams and quantification are summarized in Figure 2D.

A

Pclo	ELKS1/2	K_d(μM)	N
3623-3769	ELKS1 419-623	0.31 ± 0.06	2.38
	ELKS2 415-619	3.07 ± 0.25	2.67

B

Pclo	ELKS1-CC	K_d(μM)	N
3623-3769		0.31 ± 0.06	2.38
3644-3769		0.33 ± 0.08	1.89
3668-3769	419-623	0.20 ± 0.03	1.95
3683-3769		0.53 ± 0.10	1.75
	436-623	0.63 ± 0.19	2.14
	469-623	0.24 ± 0.10	2.15
3683-3769	510-623	1.80 ± 0.12	1.56
	469-610	0.25 ± 0.02	2.05

C

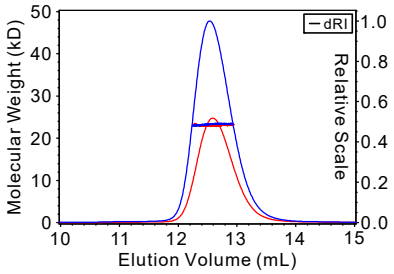

Trx-Pclo-CC3 (3683-3769)	Theoretical MW(kD)	Measured MW(kD)	Stoichiometry
100 μM	24.8	23.1 ± 0.4	monomer
200 μM	24.8	23.3 ± 0.1	monomer

Figure S4. Characterization of the Pclo-CC3/ELKS-CC interaction, related to Figure 3

(A) ITC-based measurement of the interactions between Pclo and ELKS1 or ELKS2. Binding affinity (K_D) and stoichiometry (N) are reported.

(B) ITC-based binding mapping of the interaction between Pclo and ELKS1.

(C) SEC-MALS experiment showing that Pclo-CC3 is a stable monomer at two different concentrations.

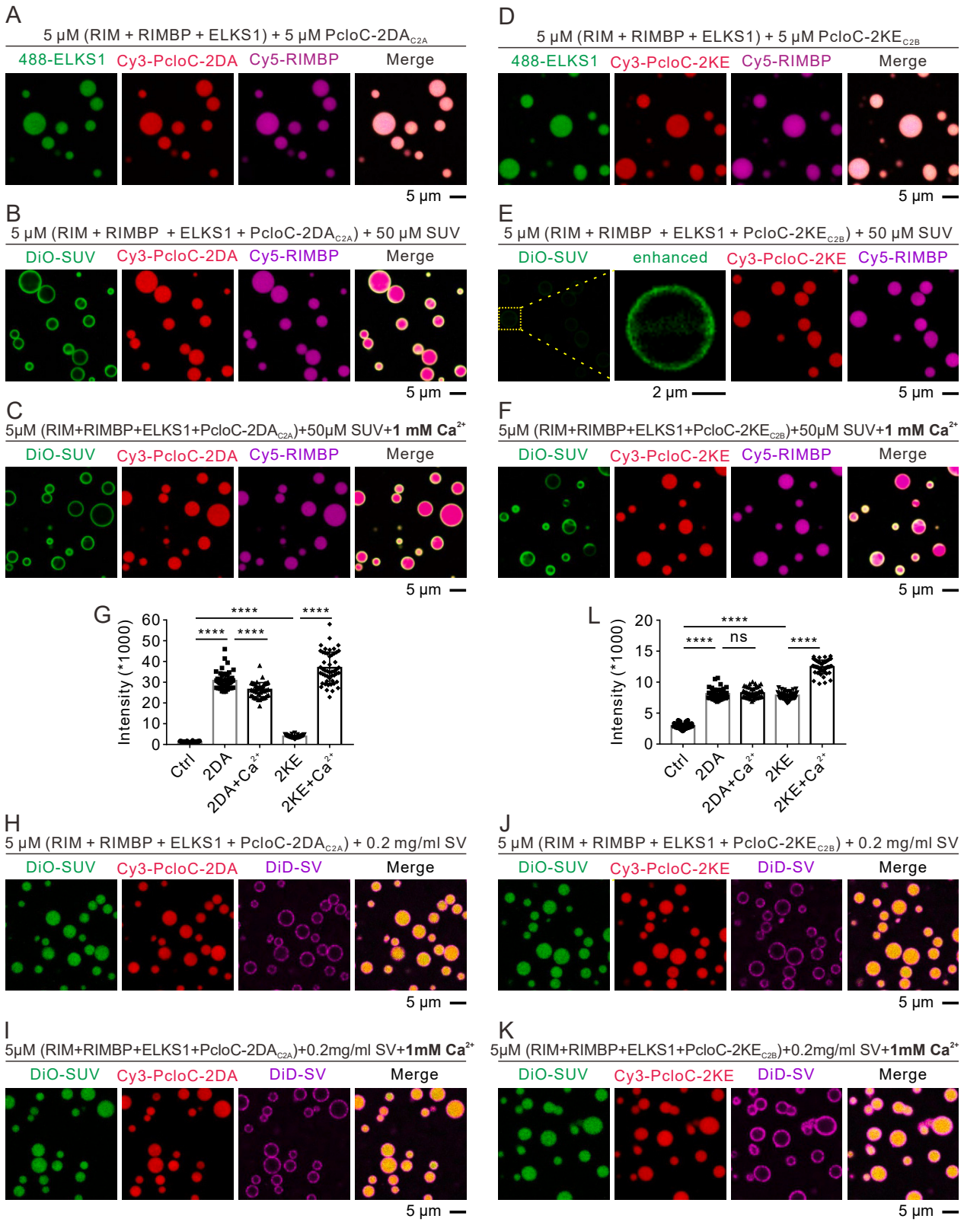

(legend on next page)

Figure S5. Characterizations of the PcloC-2DA$_{C2A}$ and PcloC-2KE$_{C2B}$ mutants reveal that both the C2A and C2B domains of Pclo contribute to Ca^{2+}-mediated vesicle tethering with the active zone condensate, related to Figure 5

(A) Representative confocal images showing that the PcloC-2DA$_{C2A}$ mutation, compared with WT PcloC, did not affect its enrichment in the RIM/RIMBP/ELKS1 condensate.

(B and C) Representative confocal images showing that SUVs coat on the surface of the RIM/RIMBP/ELKS1/PcloC-2DA$_{C2A}$ droplets in the absence (B) or presence of 1 mM Ca^{2+}.

(D) Representative confocal images showing that the PcloC-2KE$_{C2B}$ mutation did not affect its enrichment in the RIM/RIMBP/ELKS1 condensate when compared with WT PcloC.

(E and F) Representative confocal images showing that SUVs coat on the surface of RIM/RIMBP/ELKS1/PcloC-2KE$_{C2B}$ droplets in the absence (B) or presence of 1 mM Ca^{2+}.

(G) Quantification and comparison of SUV tethering efficiency of the RIM/RIMBP/ELKS condensates containing PcloC-2DA$_{C2A}$, PcloC-2KE$_{C2B}$, and the control with no PcloC, respectively, with the presence or absence of 1 mM Ca^{2+}. Data are presented as mean ± SD. For the comparisons, a one-way ANOVA with Dunnett's multiple comparisons test was used. ns, not significant, $p > 0.05$; ****$p < 0.0001$.

(H and I) Representative confocal images showing that SVs coat on the surface of the RIM/RIMBP/ELKS1/PcloC-2DA$_{C2A}$ droplets in the absence (H) or presence of 1 mM Ca^{2+} (I).

(J and K) Representative confocal images showing that SVs coat on the surface of the RIM/RIMBP/ELKS1/PcloC-2KE$_{C2B}$ droplets in the absence (J) or presence of 1 mM Ca^{2+} (K).

(L) Quantification and comparison of SV tethering efficiency of the RIM/RIMBP/ELKS condensates containing PcloC-2DA$_{C2A}$, PcloC-2KE$_{C2B}$, and the control with no PcloC with the presence or absence of 1 mM Ca^{2+}. The statistical methods are the same as in (G).

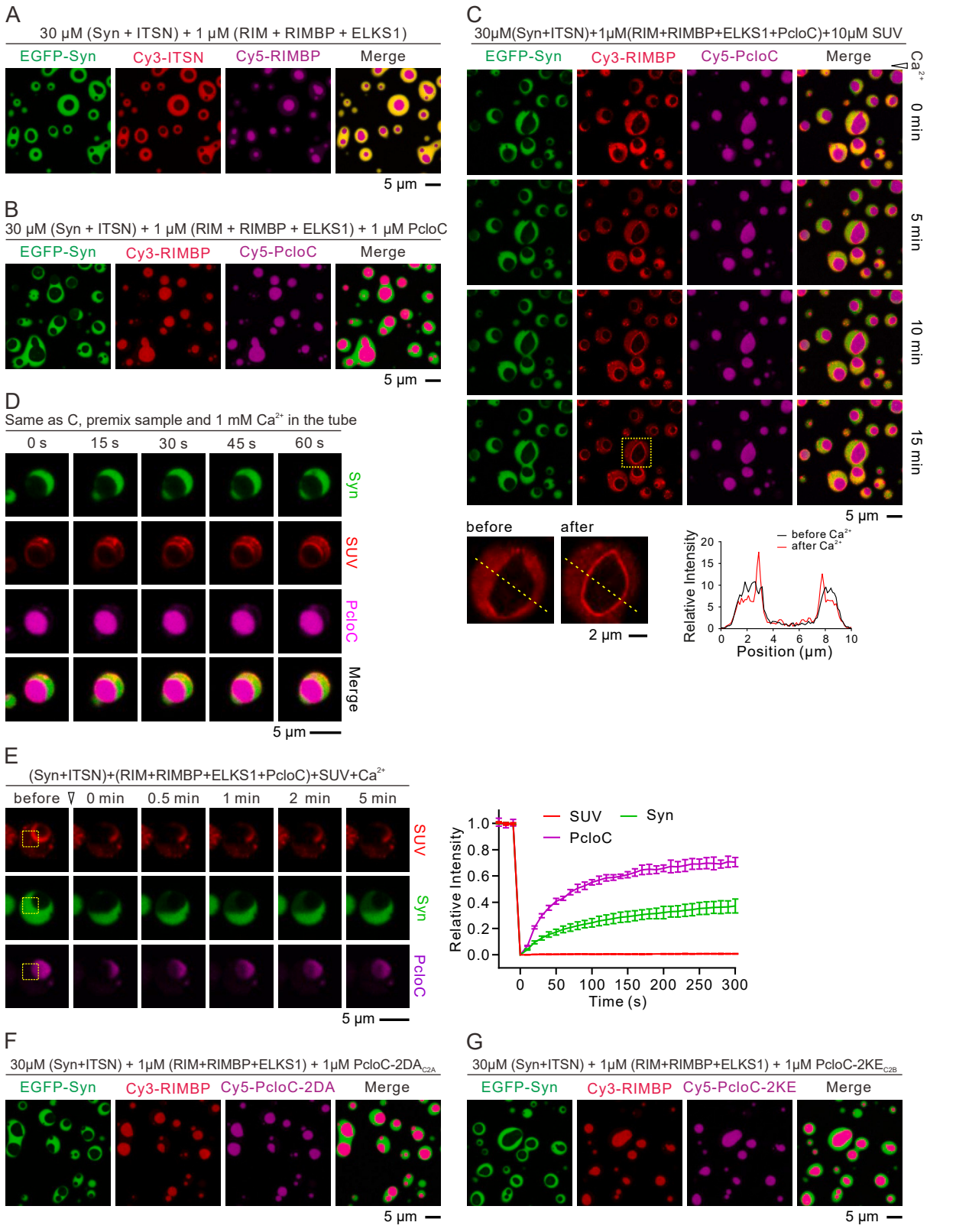

(legend on next page)

Figure S6. PcloC regulates vesicle distribution but does not affect the active zone condensate and the synapsin condensate organization, related to Figure 6

(A) Representative images showing that the RIM/RIMBP/ELKS1 condensate and the synapsin/ITSN condensate are immiscible.

(B) Representative images showing that addition of PcloC did not affect the multiphase organization of the RIM/RIMBP/ELKS1 condensate and the synapsin/ITSN condensate. PcloC was highly enriched in the RIM/RIMBP/ELKS1 condensate but not in the synapsin/ITSN condensate.

(C) Time-lapse images showing the translocation of SUVs from the synapsin/ITSN condensate to the surface of the RIM/RIMBP/ELKS1/PcloC droplets triggered by 1 mM Ca^{2+} injection. A zoom-in analysis of a representative droplet with line scanning is selected to show the SUV intensity changes before (black) and after (red) Ca^{2+} addition. See also Video S4.

(D) Same composition as (C), with a different way for sample preparation. All components were premixed and incubated for 15 min in a test tube. Then Ca^{2+} was added into the tube, and the sample was immediately loaded to the chamber for imaging. The "0 s" was defined as the time point when the imaging focal plane was reached. It is noted that SUVs were transported from the synapsin condensate to the active zone condensate surface at the time point 0 s.

(E) FRAP study of SUV, synapsin, and PcloC in the system described in Figure 6C. The yellow dashed boxes (20 pixel, 2.64 μm) mark the photobleaching region. Droplet number n = 6. Data are presented as mean ± SD.

(F and G) Representative images showing that, like WT PcloC in (B), addition of PcloC-2DA$_{C2A}$ (F), or PcloC-2KE$_{C2B}$ (G) did not affect the multiphase organization of the RIM/RIMBP/ELKS1 condensate and the synapsin/ITSN condensate.

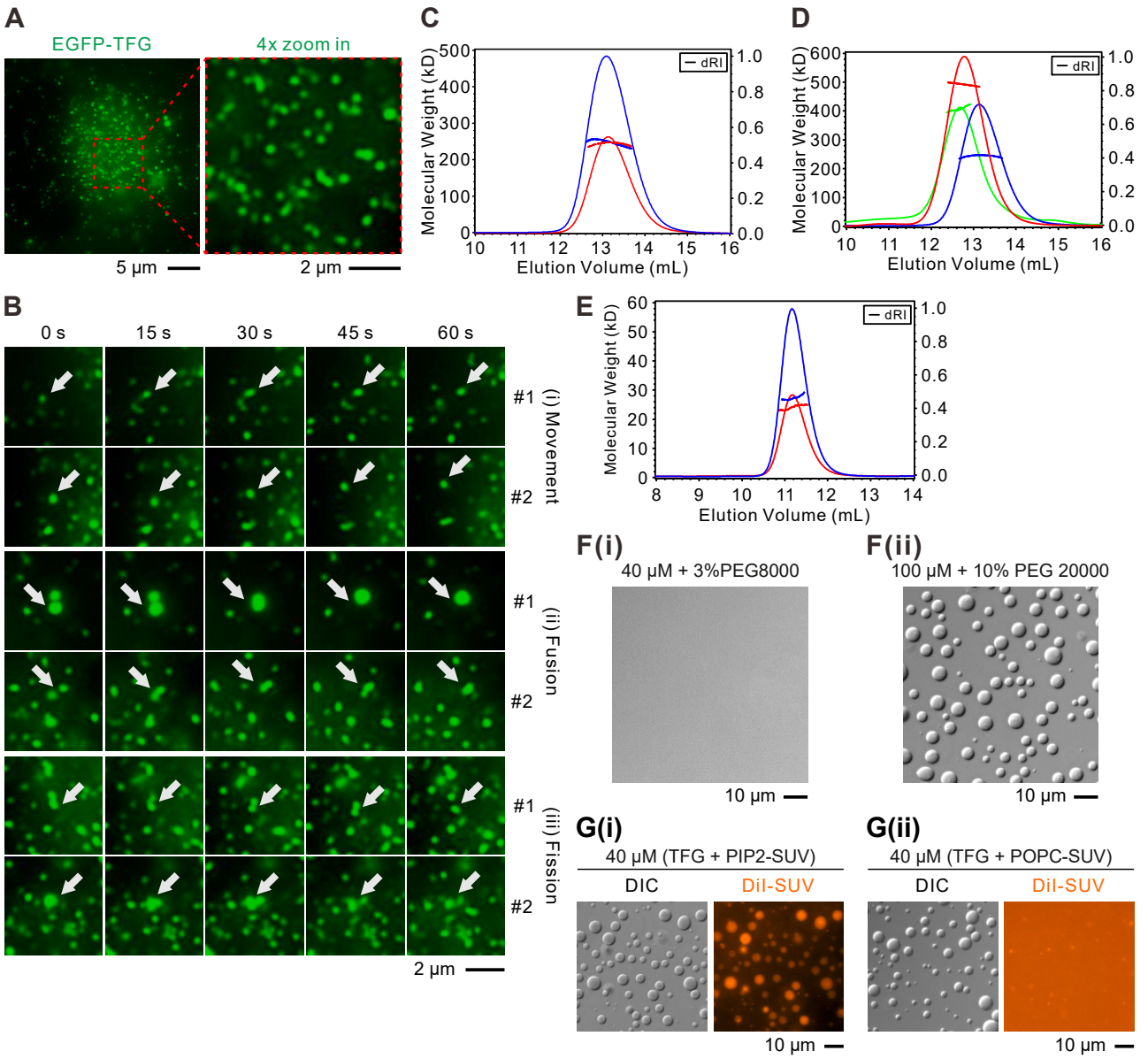

Figure S7. TFG undergoes phase separation, and the formed condensates can coacervate with negatively charged vesicles, related to Figure 7

(A) A representative image of lentivirus-infected COS7 cells stably expressing EGFP-TFG. TFG alone forms droplets in the cytoplasm.

(B) EGFP-TFG condensates formed in COS7 cells undergo dynamic change. Droplets move, fuse, and fission over time.

(C) SEC-MALS analysis of purified recombinant TFG. 40 μM (red) and 80 μM (blue) TFG were loaded into superose 6 column pre-equilibrated with TBS. Fitted molecular weights are 244.3 ± 1.5 kDa and 247.6 ± 1.2 kDa, respectively. The theoretical molecular weight of TFG is 43.4 kDa. Thus, purified TFG behaves like a stable hexamer in solution.

(D) SEC-MALS of purified recombinant EGFP-TFG and mCherry-TFG compared with untagged TFG. 40 μM EGFP-TFG (green), mCherry-TFG (red), and TFG (blue) were loaded into superose 6 column pre-equilibrated with TBS. Fitted molecular weights of EGFP-TFG and TFG are 407.4 ± 19.1 kDa and 244.3 ± 1.5 kDa, respectively, corresponding to a hexamer assembly of EGFP-TFG. mCherry has adsorption at long wavelength, where laser beam used for light scattering; thus, the molecular weight of mCherry-TFG cannot be reliably fitted. Nevertheless, the elution volume of mCherry-TFG is comparable to that of EGFP-TFG, suggesting that mCherry is also a hexamer.

(E) SEC-MALS of purified recombinant TFG-IDR. 40 μM (red) and 80 μM (blue) TFG-IDR were loaded into a superose 12 column pre-equilibrated with TBS. Fitted molecular weights are 24.1 ± 1.5 kDa and 27.3 ± 2.1 kDa, respectively. The theoretical molecular weight of TFG-IDR is 29.1 kDa. Thus, purified TFG-IDR behaves as a stable monomer in solution.

(legend continued on next page)

(F) TFG-IDR cannot undergo phase separation at the same concentration and buffer condition tested for the full-length TFG (Fi) vs. Figure 7C. Nonetheless, TFG-IDR is able to phase separate in a very high protein concentration (100 μM) and in the presence of very high molecular weight PEG (10% PEG 20,000) (Fii).
(G) The coacervation of SUV with the full-length TFG depends on negatively charged lipid. PIP2-containing SUV coacervate with TFG condensates (Gi). Whereas POPC-SUVs are not enriched by TFG condensates (Gii).